

# End-to-End Simultaneous Combined Scatter Correction and Metal Projection Segmentation for CBCT Metal Artifact Reduction Network\*

Kai Chen and Shi-peng Xie<sup>†</sup>

*School of Communications and Information Engineering,  
Nanjing University of Posts and Telecommunications, Nanjing 210003, China*

Yuan Gao

*The Key Laboratory of Computing Power Network and Information Security, Ministry of Education,  
Shandong Computer Science Center (National Supercomputer Center in Jinan),  
and Oilu University of Technology (Shandong Academy of Sciences).Jinan 250013, China*

Jiabing Gu

*The Affiliated Hospital of Qingdao University, Qingdao 266001, China*

Yan Xi

*The Shanghai First-Imaging Information Technology Co.,Ltd., Shanghai 201315, China*

Hong-yu Gao

*Department of Pharmacy, Jinling Hospital, Affiliated Hospital of Medical School, Nanjing University, Nanjing 210096, China*

Zi-hao Wang, Zhan Wu, and Hui Tang

*Laboratory of Image Science and Technology, the School of Computer Science and Engineering, Southeast University, Nanjing 210096, China*

Yang Chen

*School of Communications and Information Engineering,  
Nanjing University of Posts and Telecommunications, Nanjing 210003,  
China, and Laboratory of Image Science and Technology,  
the School of Computer Science and Engineering, Southeast University, Nanjing 210096, China*

Cone-beam computed tomography (CBCT) is widely used for high-precision three-dimensional imaging in the field of nuclear science and technology (e.g., nuclear medicine radiation therapy, nondestructive testing of nuclear facilities). However, when patients with metal implants in their bodies are examined by CT, the projection data will be contaminated and the CT reconstruction will produce severe metal artifacts affecting the diagnostic accuracy. Therefore, developing high-performance metal artifact reduction (MAR) methods for CBCT is essential for clinical diagnosis. Some of the existing MAR methods ignore physical phenomena such as x-ray scattering during CT imaging. The remaining MAR methods utilize scattering correction as a preprocessing approach, and this non-end-to-end MAR method increases the complexity of the MAR process. In this article, we design an end-to-end MAR method that incorporates both scattering correction and metal segmentation in the projection domain in the same network, followed by morphological post-processing and metal artifact suppression. Both qualitative and quantitative results and analyses in simulated and real data sets illustrate the superiority of this end-to-end MAR method.

1

## I. INTRODUCTION

2 Cone-beam CT (CBCT)[1–5] is one of the most representative CT applications with high spatial resolution and low radiation  
3 dose, and has demonstrated high clinical value as a medical measurement instrument in the fields of dentistry and interventional  
4 medicine[6–9]. However, as shown in Fig.1 when a patient with metal implants (dental fillings or orthopedic metal medical  
5 consumables) inside the body is examined on a CT scan, severe metal artifacts can occur. Reconstructed CT images containing  
6 severe metal artifacts negatively affect subsequent clinical diagnosis. Various metal artifact correction methods have been em-  
7 ployed to eliminate metal artifacts introduced by metallic substances. The most effective way to minimize the effect of extrinsic  
8 metallic factors on CT images is to avoid dense metallic components in the object being inspected. However, metal artifacts  
9 caused by medical devices implanted in the patient, such as metal dentures, vascular stents, artificial joints, and endobronchial

\* This work was supported in part by the State Key Project of Research and Development Plan under Grant 2022YFC2401600, in part by the National Natural Science Foundation of China under Grant T2225025, in part by the Key Research and Development Programs in Jiangsu Province of China under Grant BE2021703 and BE2022768, in part by China Scholarship Council under Grant 202106090126.

† Corresponding author, 419465@njupt.edu.cn

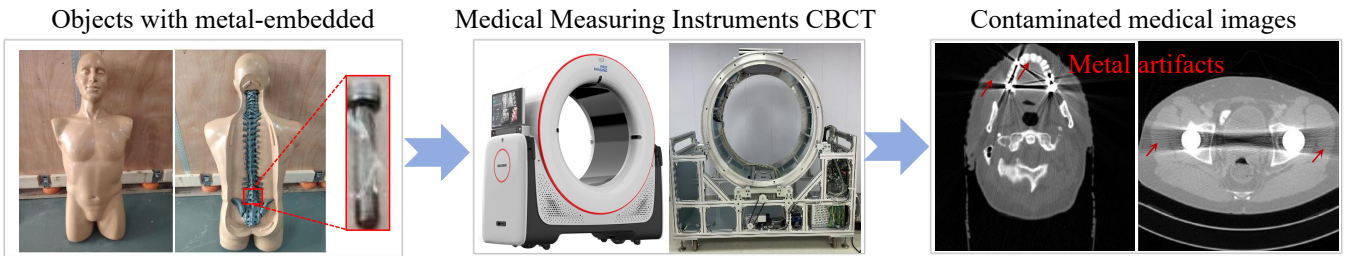


Fig. 1. CT images with severe metal artifacts after examination of patients with metallic implants within the body.

11 devices, remain unavoidable. During the data acquisition phase, another metal artifact correction strategy is to change the CT  
 12 acquisition scan acquisition parameters, such as X-ray tube voltage, tube current, scan plane, and layer thickness[10]. The  
 13 most common method is to correct for metal artifacts from the collected CT data algorithmically. These methods are roughly  
 14 categorized into three categories: MAR methods based on projection domain interpolation, MAR methods based on iterative  
 15 reconstruction, and MAR methods based on deep learning.

16 The projection data affected by metal artifacts are considered to be damaged or incomplete, and the method based on  
 17 projection domain interpolation utilizes the proximity to the complete data by interpolation to generate new projection data,  
 18 reconstructs the repaired data, and finally obtains the artifact-corrected CT image. Kalender et al.[11] proposed a Linear In-  
 19 terpolation(LI) correction algorithm to manually segment metal objects and replace the segmented metal regions using linear  
 20 interpolation. The LI is simple and fast, but secondary artifacts may occur due to segmentation conditions. In 2004, Wei et  
 21 al.[12] proposed an artifact correction algorithm based on threshold segmentation to address the shortcomings of manually  
 22 segmented regions, and used a polynomial interpolation technique to suppress metal artifacts near bones by replacing metal  
 23 pixels with polynomial interpolations of neighboring data. The method improves the accuracy of region delineation and more  
 24 effectively resolves artifacts from metals and bones, but there are still more serious secondary artifacts in the corrected results.  
 25 In 2010, Meyer et al.[13] proposed Normalized Metal Artifact Reduction (NMAR), a correction method that normalizes a priori  
 26 projection data. The NMAR method can recover the organizational details of metal boundaries and suppress the generation of  
 27 secondary artifacts. To recover the fine structure around the metal implant, Meyer et al.[14] further fused the original projection  
 28 with different weighting coefficients and the NMAR projection, and proposed the Adaptive Normalized Metal Artifact Reduc-  
 29 tion (ANMAR) algorithm to improve the NMAR. Bannas et al. [15] proposed the MAR algorithm based on image-constrained  
 30 compressed perception, which utilizes an iterative compressed perception reconstruction technique to obtain a priori images,  
 31 and constrains the estimated missing information by a priori images to improve the image quality. The MAR method based on  
 32 projection domain interpolation effectively suppresses most of the metal artifacts by interpolating the complementary projec-  
 33 tion data. It is the most commonly used and widely developed method in MAR. However, there is the problem of inaccurate  
 34 segmentation of the metal region and the inherent properties of the interpolation algorithm that may introduce new secondary  
 35 artifacts.

36 The iterative reconstruction method is based on establishing a difference function between the artifact-free CT image and the  
 37 actual acquired CT image, and then correcting and evaluating the iterative results by minimizing the objective function to obtain  
 38 the reconstructed image that is closest to the artifact-free image. Wang et al.[16] proposed two iterative reconstruction methods  
 39 for correcting metal artifacts based on the maximum expectation formula and the Algebraic Reconstruction Technique (ART).  
 40 The computational complexity of these two methods was basically the same, with the same number of iterations, the former  
 41 obtained a reconstructed image with higher clarity, but with larger noise. Beekman et al.[17] combined the Ordered Subsets  
 42 acceleration algorithm with EM algorithm and proposed Ordered Subsets Expectation Maximization (OSEM) for MAR, which  
 43 reconstructed images with better quality and improved the convergence speed of the algorithm. Chang et al.[18] proposed  
 44 an a priori-based iterative metal artifact correction method that combines the advantages of statistical methods with sinogram  
 45 interpolation methods for estimating and correcting metal-induced bias. The quality of their reconstructed images was improved  
 46 compared to the conventional NMAR and MBIR methods. Zeng et al.[19] proposed an iterative metal artifact correction method  
 47 for the projection domain based on minimizing the full variance and negative pixel energy. The iterative reconstruction method  
 48 has strong noise immunity and can directly correct metal artifacts, but its algorithm steps are complex, the computation is large,  
 49 and the iteration takes a long time.

50 Recently, DL-based algorithms have attracted great attention in medical image processing[20–23]. Deep learning-based  
 51 MAR methods can work in the sinogram domain, image domain, and simultaneously. The deep learning-based sinogram  
 52 domain MAR method[24–26] utilized a neural network to restore the metal-affected projection data directly and then recon-  
 53 structed the restored projection data into CT images. The image domain-based MAR method utilizes neural networks to map  
 54 metal-damaged CT images to clean CT images directly[27–30]. Dual-domain-based deep learning MAR network work simul-  
 55 taneously eliminates metal artifacts in the projection and image domains[31–35]. **Previous work is limited by the fact that:**  
 56 (1)Previous studies have neglected the physical processes (photoelectric effect and scattering) that occur when X-ray photons

57 interact with an object, and have studied MAR as if it were merely image processing. The presence of metallic implants worsens  
 58 the physical reaction of X-ray photons with matter, resulting in significant fragmentation of the projection data at the boundaries  
 59 of the metal trajectories in the projection domain. (2)The MAR method of dealing with metal artifacts by slice has limitations  
 60 in terms of three-dimensional spatial continuity when dealing with metal artifacts. Although it achieves better suppression on  
 61 individual slices, this method ignores the correlation between each slice, and metal artifacts can still be observed in the coronal  
 62 and sagittal planes. (3)Few MAR methods that take scattering correction into account separate scattering correction outside the  
 63 MAR framework. The removal of scattering before metal artifact suppression is performed in a way that is not an end-to-end  
 64 integrated operation, increasing the process complexity of the processing. **In this paper, we make the following contributions:**

- 65 • We have deeply investigated the physical process of CT imaging with metallic substances and X-ray photons, detailed  
 66 analysis of the causes of metal artifacts - scattering and beam hardening, and given a solution for MAR from the perspec-  
 67 tive of the principle mechanism.
- 68 • An integrated MAR framework with end-to-end scattering correction combined with metal projection segmentation is  
 69 proposed to improve the MAR performance while reducing the computational complexity and improving the efficiency  
 70 of MAR.
- 71 • Fine-grained morphological processing after metal projection segmentation is specifically designed to address pixel mis-  
 72 classification, and further optimizes the boundaries of the metal mask to ensure that they are both precise and continuous.
- 73 • The two-dimensional Delaunay triangulation interpolation restoration introduced by the proposed method effectively  
 74 preserves the rich details of the tissue structure around the metal and also reduces the residual metal artifacts in the  
 75 sagittal view. Qualitative and quantitative results on simulated and real datasets demonstrate the excellent MAR effect of  
 76 the proposed method.

77 The rest of this paper is organized as follows. Section II gives the mathematical model and the details of the neural network  
 78 architecture. The result and analysis are presented in section III. Section IV will discuss relevant issues and present conclusions.

## 79 II. METHODOLOGY

### 80 A. Principles and mechanisms of metal artifact generation

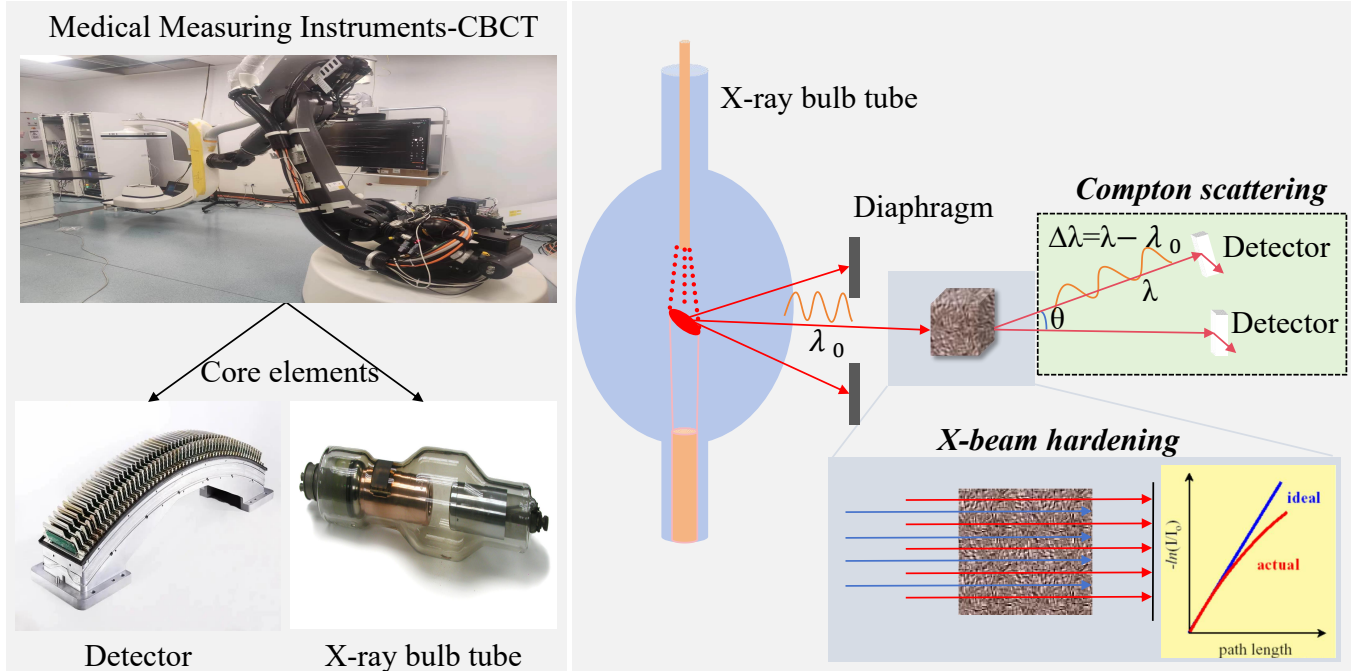


Fig. 2. Scattering and beam hardening are important factors in suffering from metal artifacts

81

### 1. Effect of scattering correction on MAR

82 When the X-rays emitted by the X-ray bulb, the core element of the medical measuring instrument CT, penetrate an object,  
 83 the photons of the X-rays received by the detector are not only the initial photons but also the scattered ones, which distorts the  
 84 measured values. This phenomenon is known as, Compton scattering, the main cause of metal artifacts, is shown in Fig.2. The  
 85 following equation can describe compton scattering:

$$86 \quad \lambda - \lambda_0 = \frac{h}{mc}(1 - \cos \theta) \quad (1)$$

87 where  $\lambda$  is the scattering wavelength,  $\lambda_0$  is the wavelength before Compton scattering occurs,  $h$  is Planck's constant,  $m$  is the  
 88 electron mass,  $c$  is the speed of light, and  $\theta$  is the angle of rotation of the photon direction. From Eq.1, it can be seen that the  
 89 probability of Compton scattering occurring is directly related to the electron density in the material, which is then associated  
 90 with the atomic number of the substance. The scattering effects of metallic substances are again different relative to tissue  
 91 and bone due to their high atomic numbers. Further, Fig.3 and Fig.4 visualize the effect of the presence of scattering on the  
 92 MAR. The overall contrast of the image was dark when scatter correction was not performed, some tissues and bones were  
 93 difficult to observe, and some tissue details were lost ( slice 1 and slice 3 in Fig.3). For slice 3 of Fig.4, the blurring around the  
 94 metallic substance within the ROI before scatter correction severely affects the quality of the image. The enhancement of bone  
 95 contrast within the ROI after scatter correction also restored the apparent artifacts within the ROI. In summary, the occurrence  
 96 of scattering phenomena during CT examination of objects containing metal inlays can strongly exacerbate the generation of  
 97 metal artifacts, which manifests itself as a reduction in the overall contrast of the CT image and causes artifacts.

100

### 2. Effect of beam hardening on MAR

101 As shown in Fig.2, CT, a clinically used medical measurement instrument, usually employs an X-ray beam energy spectrum  
 102 containing photons of different energies to obtain high-quality CT images. As a multi-energy X-ray beam passes through the  
 103 object being scanned, the lower energy photons are preferentially attenuated, while the higher energy photons are not as easily  
 104 attenuated. As a result, the average energy (hardness) of the beam increases as the rays penetrate more of the material, as  
 105 evidenced by an increase in the proportion of high-energy photons relative to low-energy photons, a phenomenon known as  
 106 beam hardening. When the reconstruction is performed using the algorithm, a large number of black streak artifacts appear at  
 107 the metal locations in the reconstructed image (Fig.5(right)), which are beam-hardening artifacts, is the most important reason  
 108 for the appearance of metal artifacts. Considering the presence of metallic substances in the scanned object, the scattering  
 109 kernel widths of the metallic substances are different in size from the scattering widths of the body tissues, so we designed a  
 110 three-output scattering correction network for metallic substance projections.

112

## B. End-to-end combined scattering correction and metal projection segmentation in integrated MAR scheme

113 We propose a framework for simultaneous scattering correction and metal projection segmentation for MAR as shown in  
 114 Fig.6. The inputs to the framework are the CBCT projection and the air projection after the logarithmic operation. The in-  
 115 put data is corrected on the one hand by a scattering correction network for the projection, then the projection is corrected  
 116 by Empirical Beam Hardening Correction(EBHC)[36], next FDK reconstructs the corrected projection, and threshold segmen-  
 117 tation(TS) is performed. Finally, these metal regions are projected forward from the image domain to the sinogram domain  
 118 using the forward projection algorithm (FP). On the other hand, the corrected projection data and the air projection are fed into  
 119 a metal projection segmentation network to segment out metal regions in the projection domain. Morphological fine-tuning  
 120 of segmented metal projections employing forward projection. The projections are then inpainted by Delaunay triangulation  
 121 interpolation to eliminate metal artifacts and reconstruct high-quality CBCT images, and finally, metal backfilling(MB) is per-  
 122 formed.

123 This scattering correction network employs a classical coding-decoding architecture that simultaneously outputs the scat-  
 124 tering amplitude matrix, the convolutional Gaussian kernel parameters, and the convolutional kernel selection matrix. The  
 125 convolutional scattering amplitude matrix selects scattering kernel parameters adapted to the properties of different metal re-  
 126 gions, accurately estimates the scattering signals in different regions, and effectively captures the diversity of scattering signals  
 127 due to material differences. The convolutional kernel selection matrix is devoted to outputting a matrix that matches the size  
 128 of the input image to facilitate the selection of Gaussian kernel parameters that can determine the determination of that pixel  
 129 point, automatically learning and determining the optimal Gaussian kernel parameter for each pixel to optimize the processing  
 130 of the scattering signal. The results of the estimation and correction of the scattered signal are based on the learned scattering  
 131 amplitude matrix  $c(x, y)$ , 8 pairs of Gaussian kernel parameters  $\sigma_1$  and  $\sigma_2$ , the categorization indicator function  $M^i(x, y)$  de-  
 132 termined by the Gaussian kernel selection matrix and the total detected signal  $I(x, y)$ , and the total computational procedure is  
 133

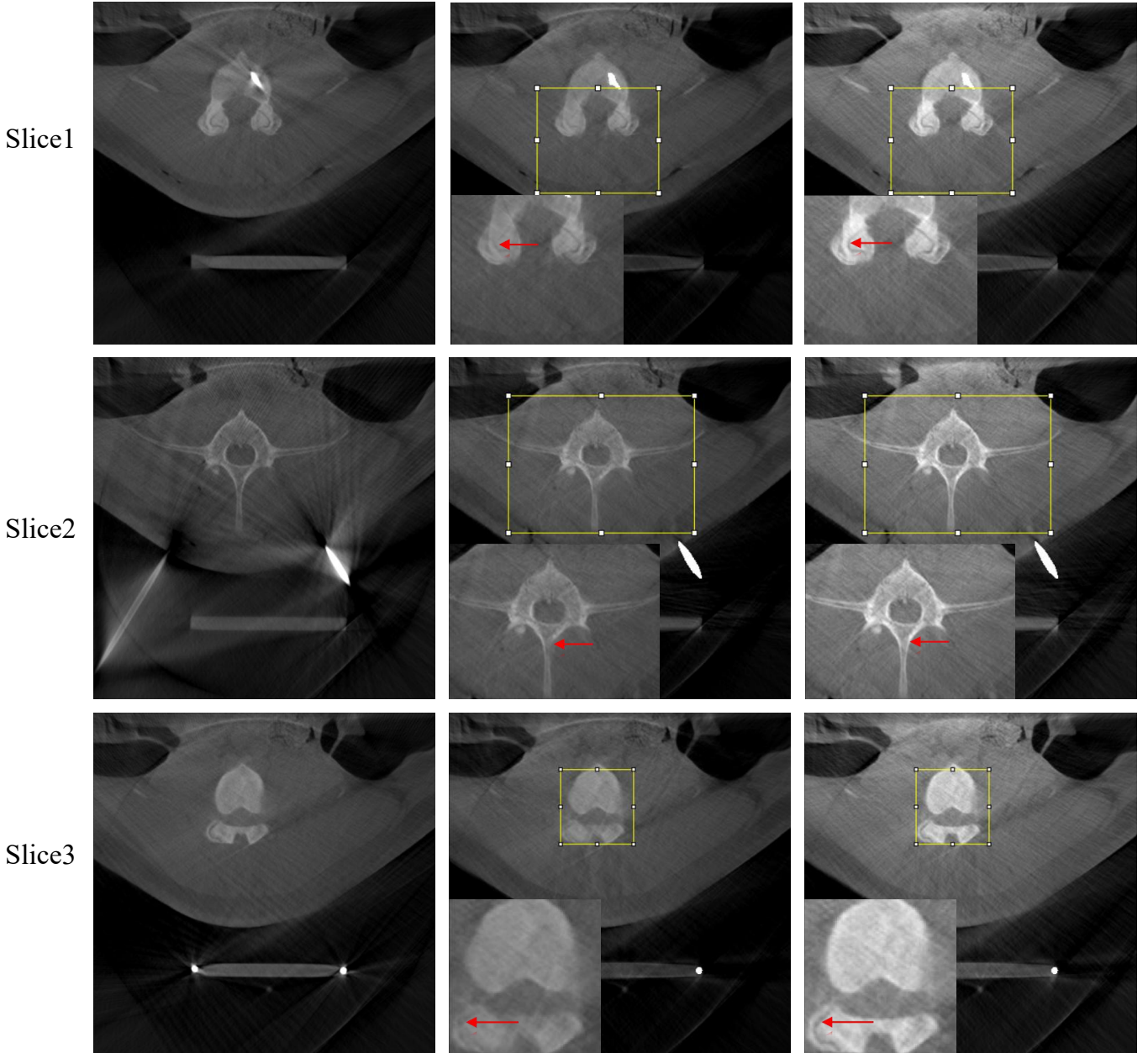


Fig. 3. The first column shows the image without scattering suppression and without metal artifact suppression, the second column shows the effect of no scattering correction but metal artifact suppression, and the third column shows the result of metal artifact suppression with both scattering correction. The display window is [200, 2000] HU.

134 illustrated in the following equation.

$$135 \quad I_s = \sum_i F^{-1} [\mathcal{F}(I(x, y)c(x, y)) M^i(x, y) \mathcal{F}(g^i(x, y))] \quad (2)$$

136 The computational process of scattering correction is graphically demonstrated in Fig. 7. The metal projection segmentation  
 138 network adopts the U-Net architecture as shown in Fig.6, which mainly consists of up-sampling and down-sampling. The  
 139 loss function of the simultaneous scattering correction and metal projection segmentation network is given by the following  
 140 equation:

$$141 \quad Loss = -\frac{1}{N} \sum_{i=1}^N [y_i \log(p_i) + (1 - y_i) \log(1 - p_i)] \quad (3)$$

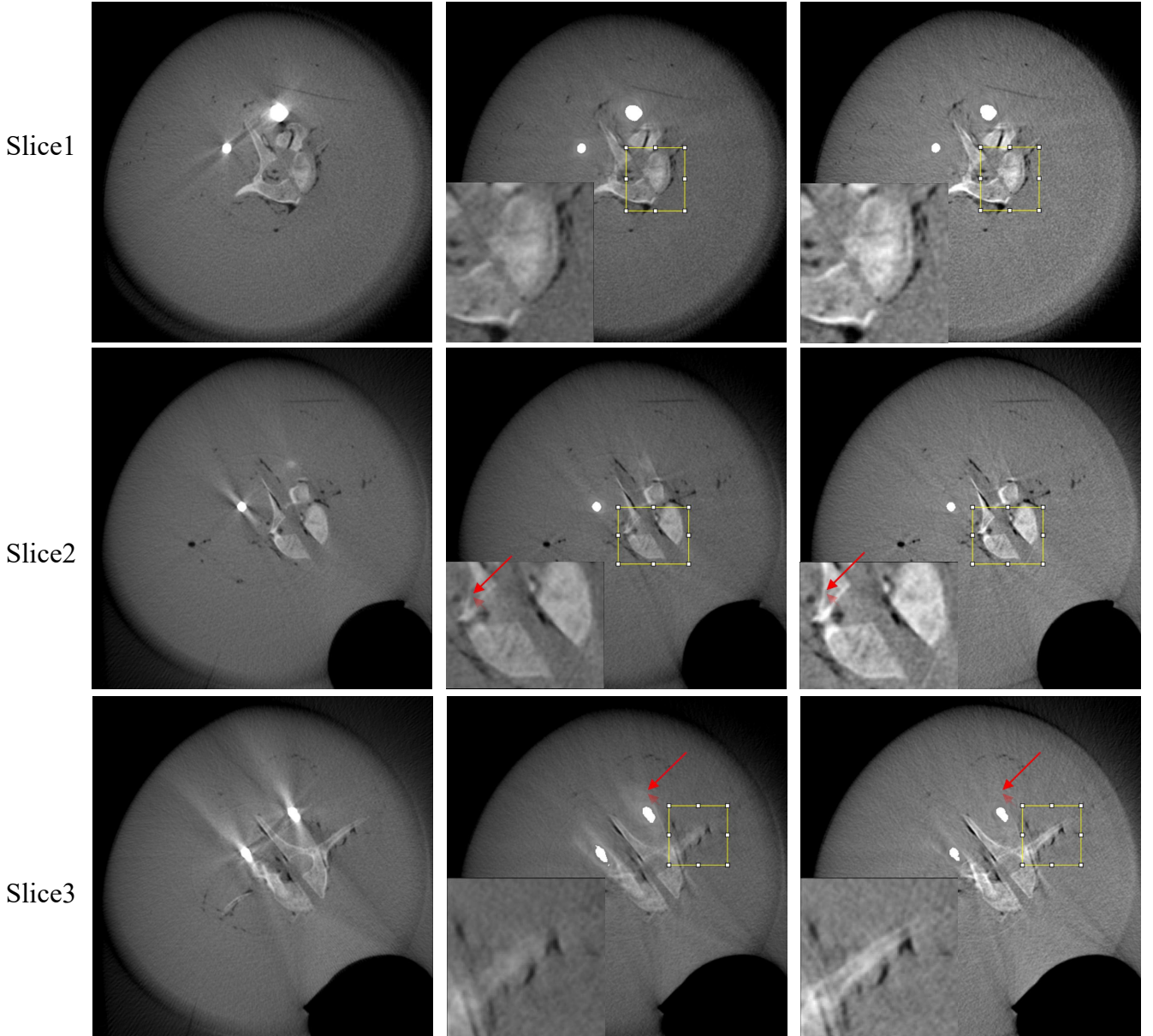


Fig. 4. The first column shows the image without scattering suppression and without metal artifact suppression, the second column shows the effect of no scattering correction but metal artifact suppression, and the third column shows the result of metal artifact suppression with both scattering corrections. The display window is [140, 1300] HU.

142 Where  $N$  is the number of pixels in the image,  $y_i$  is the true label of the  $i$ th pixel, takes the value 0 or 1,  $p_i$  and is the probability  
 143 that the  $i$ th pixel is a positive class as predicted by the network.

144

### C. Refinement of metal projection after segmentation

145 After obtaining the metal projection segmentation results, misclassification of some pixels may occurred during the segmen-  
 146 tation process as shown in Fig.8. As can be seen in Fig.8, some regions within the projection data are incorrectly labeled as  
 147 metals. Therefore, it is not sufficient to obtain the metal segmentation results of the projected domain of the network, but these  
 148 segmentation results must also be fine-tuned.

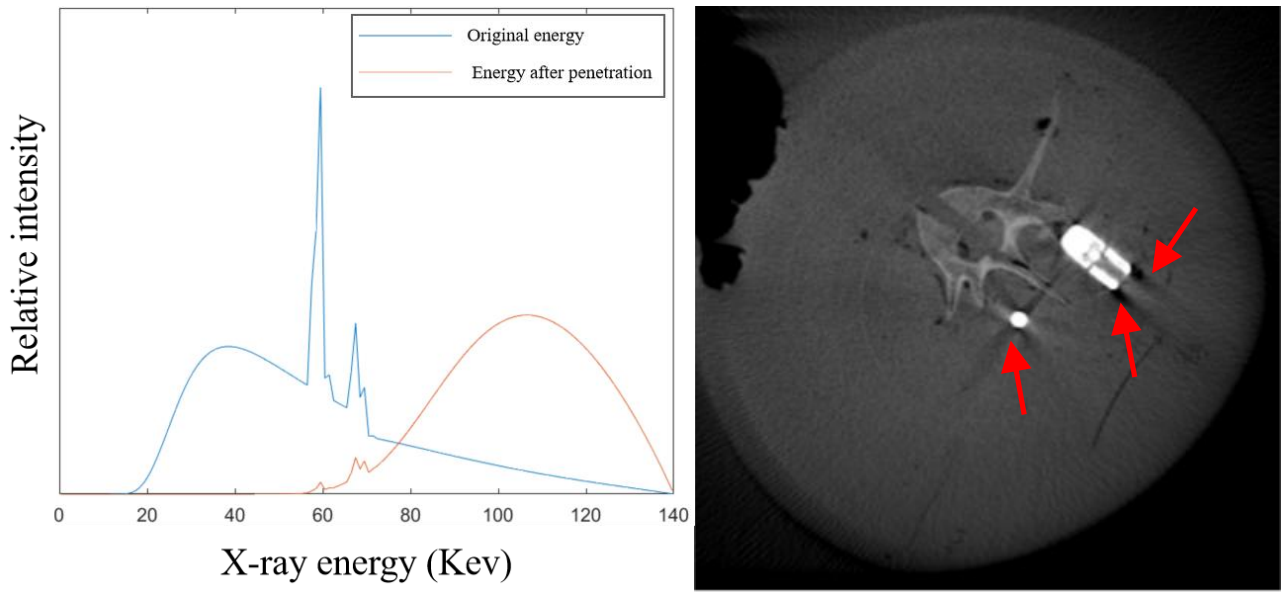


Fig. 5. Effect of beam hardening on MAR. Initial and final energy intensity of X-rays as they pass through an object(left), artifacts caused by beam hardening(right).

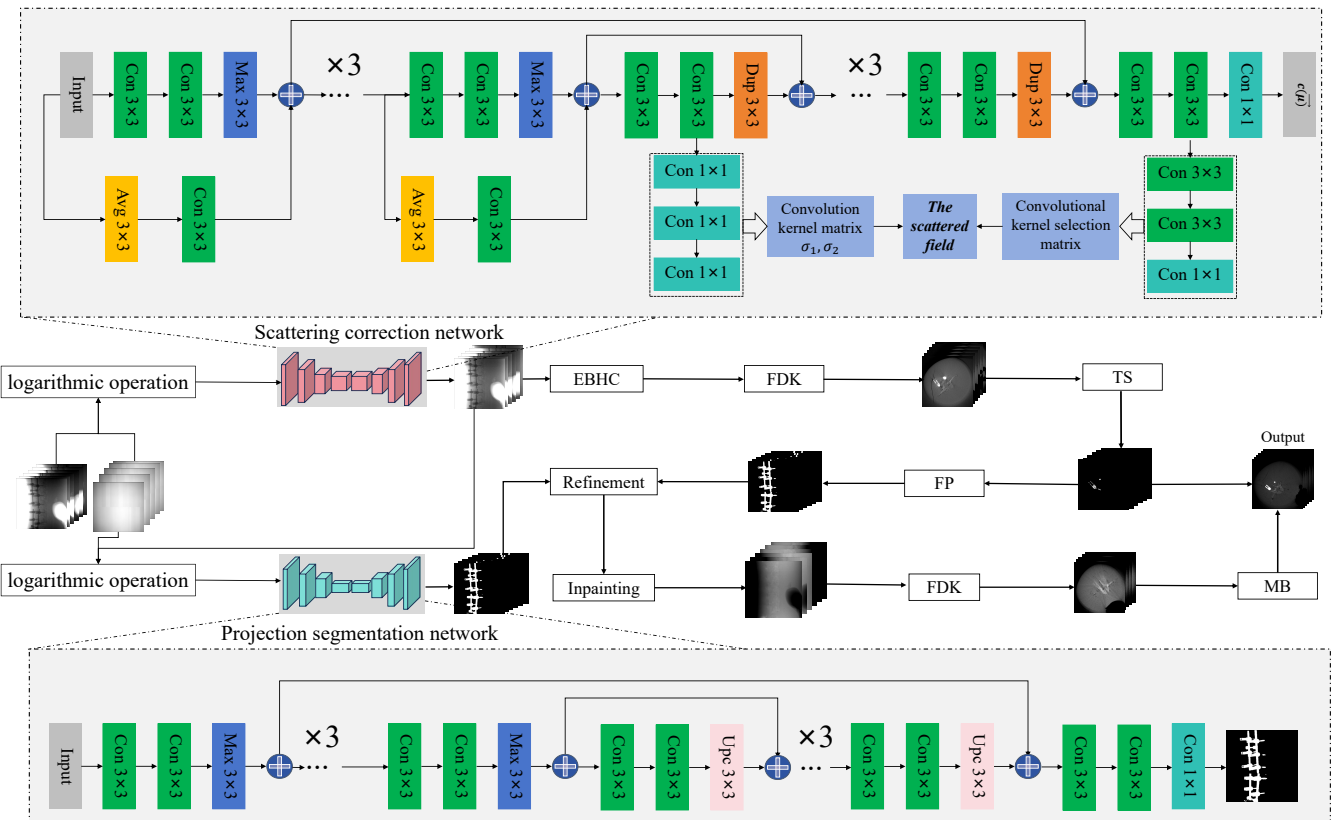


Fig. 6. A framework for simultaneous scattering correction and metal projection segmentation for MAR.

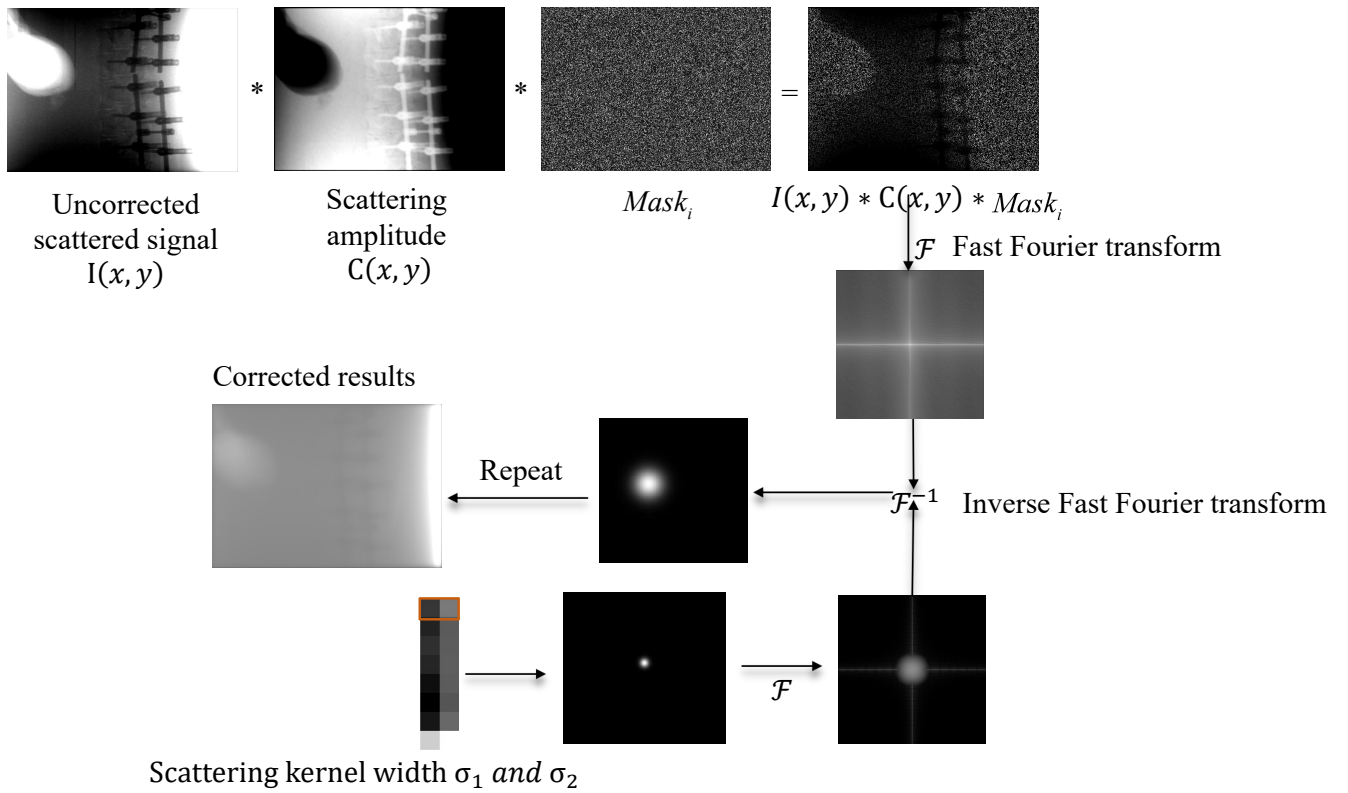


Fig. 7. Calculation procedure for scattering.

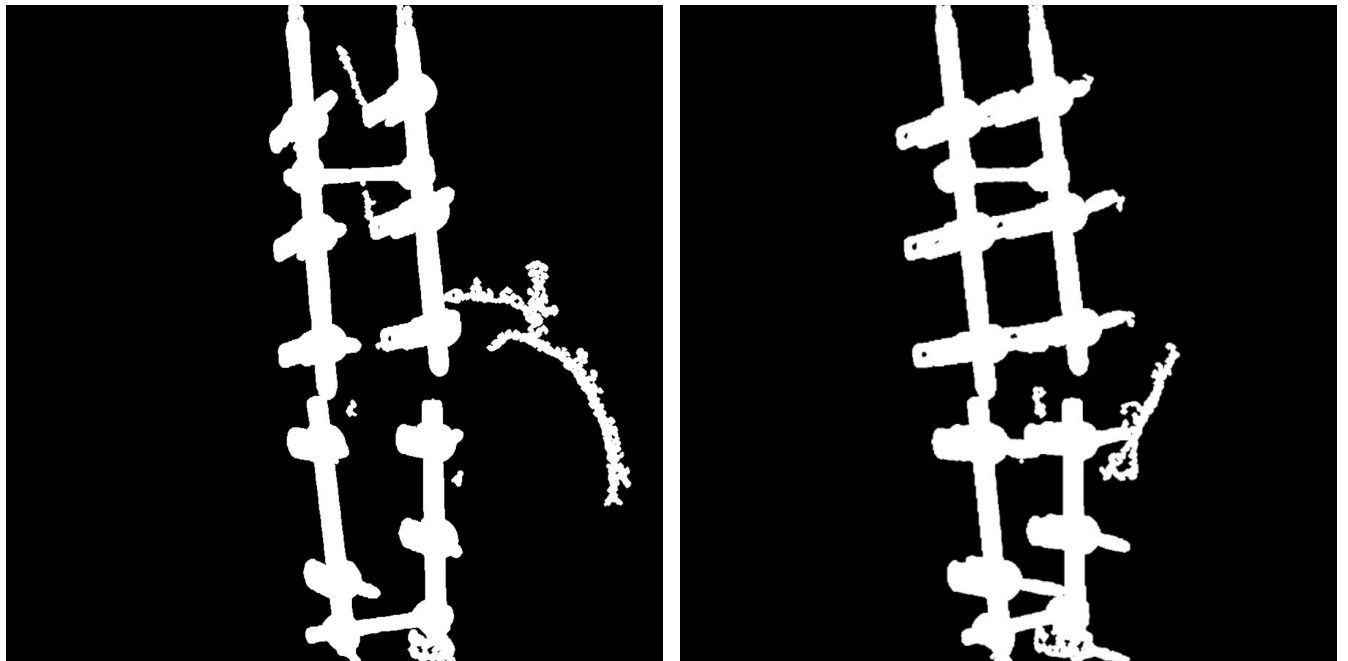


Fig. 8. Misclassification in metal projection segmentation results.

---

**Algorithm 1** Metal Artifact Reduction via Dual-Threshold Projection Refinement

---

**Require:** Reconstructed volume  $\mathbf{V} \in \mathbb{R}^{N_x \times N_y \times N_z}$   
**Ensure:** Refined segmentation mask  $\mathbf{M}_{\text{final}} \in \{0, 1\}^{N_x \times N_y}$

```

1: Initialize projection index:  $p \leftarrow 1$ 
2: repeat
3:    $\mathbf{P}_p \leftarrow \mathcal{F}_{\text{FP}}(\mathbf{V}_p)$  ▷ Forward projection
4:   COARSE SEGMENTATION:
5:    $\mathbf{M}_1^{(p)} \leftarrow \mathcal{T}_{\theta_1}(\mathbf{P}_p)$  ▷ High sensitivity threshold  $\theta_1$ 
6:   FINE SEGMENTATION:
7:    $\mathbf{M}_2^{(p)} \leftarrow \mathcal{T}_{\theta_2}(\mathbf{P}_p)$  ▷ High specificity threshold  $\theta_2$ 
8:   NEURAL PRIOR INTEGRATION:
9:    $\tilde{\mathbf{M}}^{(p)} \leftarrow \mathcal{N}(\mathbf{P}_p) \vee \mathbf{M}_1^{(p)}$  ▷ Neural network operator  $\mathcal{N}$ 
10:  CONSENSUS REFINEMENT:
11:    $\mathbf{M}_{\text{refined}} \leftarrow \tilde{\mathbf{M}}^{(p)} \wedge \mathbf{M}_2^{(p)}$ 
12:  GEODESIC PROPAGATION:
13:    $\mathbf{M}_{\text{final}}^{(p)} \leftarrow \mathcal{G}(\mathbf{M}_{\text{refined}}, \mathbf{P}_p)$ 
14:    $p \leftarrow p + 1$ 
15: until  $p > N_{\text{proj}}$  ▷ Total projections:  $N_{\text{proj}}$ 

```

---

150 In the original uncorrected reconstructed images, two critical thresholds, denoted as *Thres1* and *Thres2*, are established.  
151 Among these, *Thres1* is set as a higher threshold, while *Thres2* is a lower threshold. These thresholds are used to effectively  
152 segment metal masks in the image domain, serving as a foundation for subsequent processing steps. Next, forward projection  
153 techniques are applied to the segmented metal masks, converting the segmentation results from the image domain to the pro-  
154 jection domain. The resulting projections are denoted as  $P_{\text{mt1}}$  and  $P_{\text{mt2}}$ , respectively. This transformation provides the  
155 necessary data for further operations. In the subsequent steps, the network segmentation result ( $Net_{\text{mt}}$ ) is combined with  
156  $P_{\text{mt1}}$  using a logical OR operation, producing an intermediate result ( $Tmp1$ ). This operation expands the metal region to  
157 ensure that all potential metal components are included. The expanded result ( $Tmp1$ ) is then refined through a logical AND  
158 operation with  $P_{\text{mt2}}$ , effectively filtering out regions that may have been falsely identified as metal, thereby improving seg-  
159 mentation precision. Finally, a morphological region-growing operation is applied to the resulting  $Tmp2$ . This morphological  
160 process further optimizes the boundaries of the metal mask, ensuring both accuracy and continuity. By iteratively applying the  
161 entire workflow, an efficient network-threshold-based segmentation method is implemented for CBCT projections.

162 **D. Triangulation-Based Metal Artifact Suppression for CBCT MAR**

163 In the field of CBCT metal artifact suppression, linear interpolation remains a widely utilized method due to its simplicity  
164 and ease of implementation. However, this approach often results in significant detail loss, particularly in regions surrounding  
165 metallic objects. By estimating the pixel values in metal regions using the average of adjacent non-metal areas, linear inter-  
166 polation fails to preserve fine textures and intricate details, potentially introducing blurring artifacts that degrade the overall  
167 image quality. To overcome these limitations, this study proposes a triangulation-based interpolation technique that effectively  
168 repairs projection-domain images, suppresses metal artifacts, and reconstructs high-quality CBCT images. This method cor-  
169 rects the affected regions in the projection domain and subsequently restores the metal regions in the reconstructed image. The  
170 mathematical formulation of the proposed interpolation method is presented in Eq. (4):

$$P(x) = \lambda_A V_A + \lambda_B V_B + \lambda_C V_C, \quad (4)$$

171 where  $V_A$ ,  $V_B$ , and  $V_C$  denote the intensity values at the vertices  $A$ ,  $B$ , and  $C$  of a triangle in the 2D projection domain,  
172 respectively.  $P(x)$  represents the interpolated intensity value at point  $P$  within the triangle. The weights  $\lambda_A$ ,  $\lambda_B$ , and  $\lambda_C$  are  
173 the barycentric coordinates of  $P$ , satisfying the condition:

$$\lambda_A + \lambda_B + \lambda_C = 1, \quad (5)$$

174 where each  $\lambda$  quantifies the proportional contribution of the respective vertex to the interpolated value at  $P$ . The barycentric  
175 coordinates  $\lambda_A$ ,  $\lambda_B$ , and  $\lambda_C$  are derived based on geometric relationships, as described in Eq. (6):

$$\begin{aligned} \lambda_A &= \frac{S(\triangle PBC)}{S(\triangle ABC)}, \\ \lambda_B &= \frac{S(\triangle PCA)}{S(\triangle ABC)}, \\ \lambda_C &= \frac{S(\triangle PAB)}{S(\triangle ABC)}, \end{aligned} \quad (6)$$

179 where  $S(\triangle ABC)$  represents the area of the triangle formed by vertices  $A$ ,  $B$ , and  $C$ , and  $S(\triangle PBC)$ ,  $S(\triangle PCA)$ , and  
 180  $S(\triangle PAB)$  denote the areas of the sub-triangles formed by point  $P$  and the respective vertex pairs. The proposed method  
 181 employs a 2D Delaunay triangulation-based interpolation to repair the metal-corrupted regions in the projection domain. This  
 182 technique ensures that the interpolated values accurately reflect the spatial and intensity distribution of the surrounding non-  
 183 metal regions. After processing all projection images, the Feldkamp-Davis-Kress (FDK) algorithm is applied to perform 3D  
 184 image reconstruction. In the final step, the restored metal regions are seamlessly backfilled into the reconstructed image,  
 185 thereby completing the suppression of metal artifacts. Compared to traditional linear interpolation, the proposed triangulation-  
 186 based method offers significant advantages in preserving the structural details and textures near metal objects. By leveraging  
 187 barycentric coordinate-based interpolation, this approach ensures a more precise and realistic reconstruction of the projection-  
 188 domain data, leading to improved image quality in CBCT applications.

189

### III. EXPERIMENT RESULTS AND ANALYSIS

190

#### A. Experimental Setup

191 The projection domain correction network and the metal segmentation network were both implemented using the PyTorch  
 192 framework. Prior to training the full network, the scatter correction network was pre-trained to obtain an initial scatter cor-  
 193 rection model. Subsequently, the full network was trained end-to-end by jointly optimizing both the projection correction and  
 194 metal segmentation networks. The training process was conducted in a computing environment running a 64-bit Windows 10  
 195 operating system, equipped with 32 GB of RAM and an NVIDIA GeForce GTX-3090 GPU with 24 GB of video memory.  
 196 The CPU used was an Intel i5-650 processor. PyTorch was employed for all network training tasks. The Adam optimizer  
 197 was utilized with parameters  $\beta_1 = 0.5$  and  $\beta_2 = 0.99$ . A batch size of 6 was used, and the training process comprised 400  
 198 epochs. The initial learning rate was set to 0.0001 and decayed linearly starting from epoch 160 to epoch 320, following a decay  
 199 factor of  $\gamma = 0.5$ . The network training spanned 100 iterations, with a batch size of 6 and an initial learning rate of 0.0001.  
 200 The triangulation-based interpolation method for suppressing metal artifacts was implemented using MATLAB R2021a, where  
 201 computational efficiency was enhanced via the Mex compilation mechanism.

202

#### B. Datasets and Training Protocols

203 To comprehensively evaluate the proposed method for CBCT MAR, extensive simulated and clinical datasets were utilized.  
 204 Both data categories were meticulously designed to replicate realistic imaging scenarios while ensuring consistency across  
 205 experiments. Table 1 and Table 2 summarize the key acquisition parameters for simulation-based and clinical data, respectively.  
 206 The SPEKTR 3.0 toolkit was employed to generate the polychromatic energy spectrum, simulating a realistic X-ray source.  
 207 The detector dimensions were set to  $960 \times 960$  pixels with a pixel size of 0.616 mm, corresponding to a field of view (FOV)  
 208 of  $480 \times 480$  mm. Key geometric parameters included a source-to-object distance (SOD) of 612 mm and a source-to-detector  
 209 distance (SDD) of 1138 mm. A total scanning angle of  $360^\circ$  was covered with 400 evenly spaced projections.

TABLE 1. Simulation Parameters for Data Generation

Parameter	Value
Source-to-Object Distance (SOD)	612 mm
Source-to-Detector Distance (SDD)	1138 mm
Total scan angle	$360^\circ$
Total projection number	400
Detector size	$960 \times 960$
Pixel spacing	0.616 mm
Field of View (FOV)	$480 \times 480$ mm

210

211 To ensure the availability of sufficient training data, this study employed the publicly available DeepLesion dataset provided  
 212 by the Clinical Center of the National Institutes of Health (NIH) as a benchmark. A total of 20 patients' abdominal and thoracic  
 213 CT scans were selected, and soft tissue and bone structures were carefully segmented to ensure diversity. For subsequent better  
 214 removal of metal artifacts, 20 metal masks were manually designed. These were manually annotated and inserted into the  
 215 anatomical regions of 20 distinct patients within the dataset. The density and corresponding coordinates of the different tissues  
 216 were filled in the file required for the MC-GPU simulation, and the projection data for the presence and absence of scattered  
 217 signals were obtained after the simulation was completed. The photon count for the simulation was set to 105 incident photon  
 218 counts per detector pixel. The voxel size of the model was set to  $0.08 \text{ cm} \times 0.08 \text{ cm} \times 0.16 \text{ cm}$ , with a total of 400 projections  
 219 for each model. Fig.11 illustrated a sample projection was shown of a simulated dataset. The clinical data acquisition system

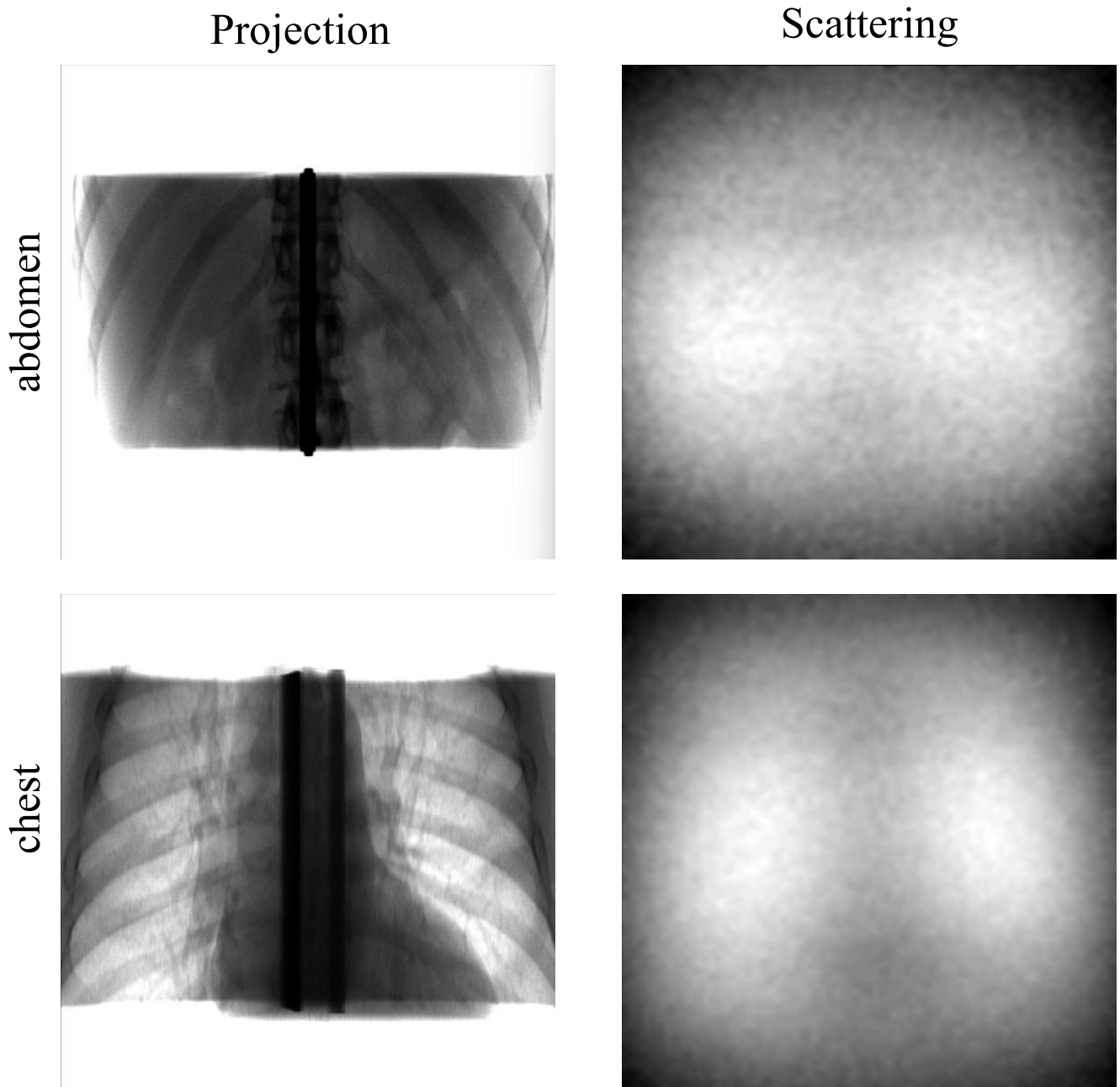


Fig. 9. A sample projection of a simulated dataset.

222 used for all experiments had a detector pixel matrix of  $960 \times 960$  and a pixel size of  $0.45 \text{ mm} \times 0.45 \text{ mm}$ . The tube voltage for  
 223 the CT scan was 80 kv and the tube current was 3 mA. The scanning angle was 360 degrees, the number of scans was 400, and  
 225 the total scanning time was 80 seconds. The reconstructed volume dimensions of the arch nail model and the human spine were  
 226  $512 \times 512 \times 512$  and  $394 \times 394 \times 300$ . All projection data were downsampled 2x to  $480 \times 480$  by bilinear interpolation prior  
 227 to input to the network and upsampled to the original size after scatter correction was completed. Fig. 11 illustrated a sample  
 228 projection was shown of a clinical dataset.

TABLE 2. Clinical Data Acquisition Protocol

Parameter	Value
Source-to-Object Distance (SOD)	612 mm
Source-to-Detector Distance (SDD)	1138 mm
Total scan angle	360°
Total projection number	400
Detector size	960 × 960
Pixel spacing	0.45 mm
Reconstruction volume	512 × 512 × 512
Physical coverage	394 × 394 × 400 mm
Scan time	80s

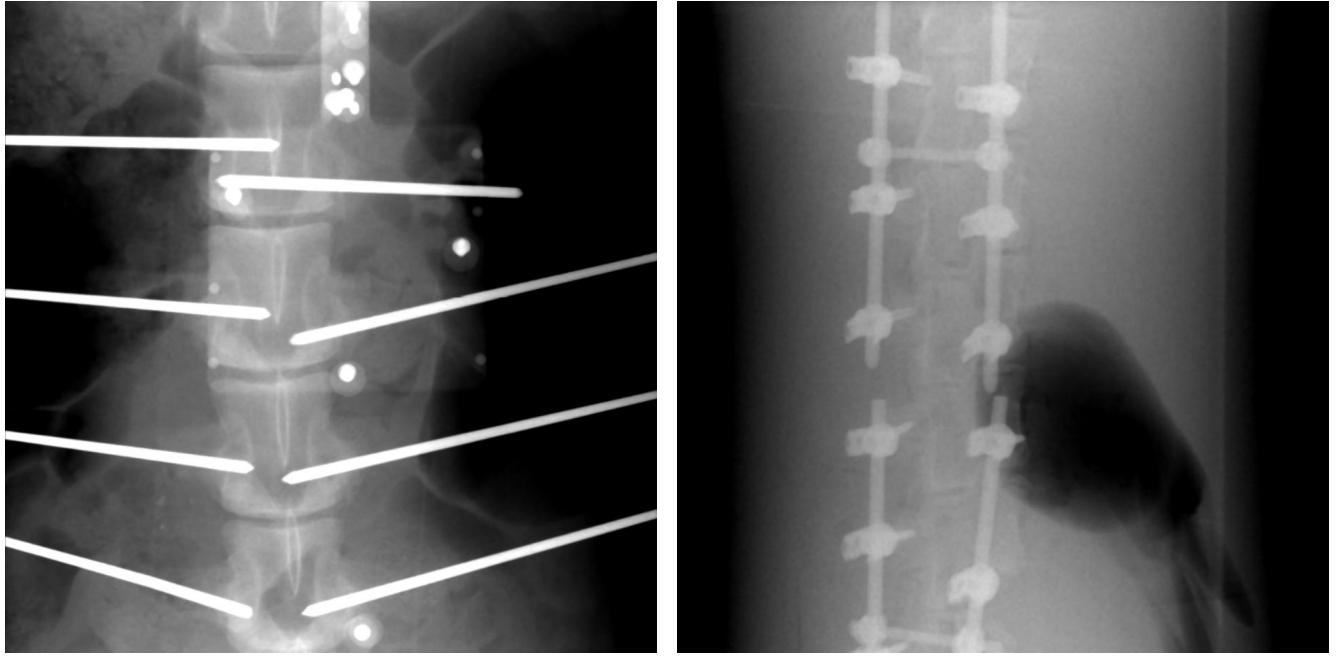


Fig. 10. A sample projection of a clinical dataset.

230

## C. Results and analysis of comparison experiments

231

### 1. Analysis of Metal Artifact Suppression Results

232 The linear interpolation[11], VMS[37] and PDS[37] are compared with the proposed method to demonstrate the superiority of  
 233 the proposed method. The MAR results of two clinical cases in different methods are shown in Fig.11, with some ROIs zoomed  
 234 in to facilitate the observation of details of some tissues and structures. Without any metal artifact correction, the artifacts caused  
 235 by metal implants dominate large portions of the tissue regions, obscuring crucial anatomical details. Additionally, severe  
 236 streaking artifacts are observed along angular views. Employing linear interpolation to correct the artifacts was ineffective for  
 237 clinical data, as this method failed to reconstruct sufficient tissue details. Specifically, most structural details in the vertebral  
 238 region were either lost or heavily distorted, while severe secondary artifacts were introduced. From angular views, residual  
 239 artifacts were also observed. The VMS method exhibited a notable improvement in suppressing metal artifacts, yielding results  
 240 comparable to the PDS method and the proposed approach in certain aspects. However, its performance was inconsistent, as  
 241 evidenced by residual metal artifacts in Slice 1. These artifacts were prominent in certain regions or angular directions, limiting  
 242 the effectiveness of VMS. The PDS method demonstrated relatively good artifact suppression in angular views. However,  
 243 it failed to preserve fine structural details in ROI. For instance, in Slice 1, the bone structures and surrounding soft tissues  
 244 within the ROI were not as well-preserved compared to the proposed method. Additionally, in Slice 2, noticeable bright spots  
 245 were observed in the vertebral region post-processing, indicating incomplete suppression of artifacts. In contrast, the proposed  
 246

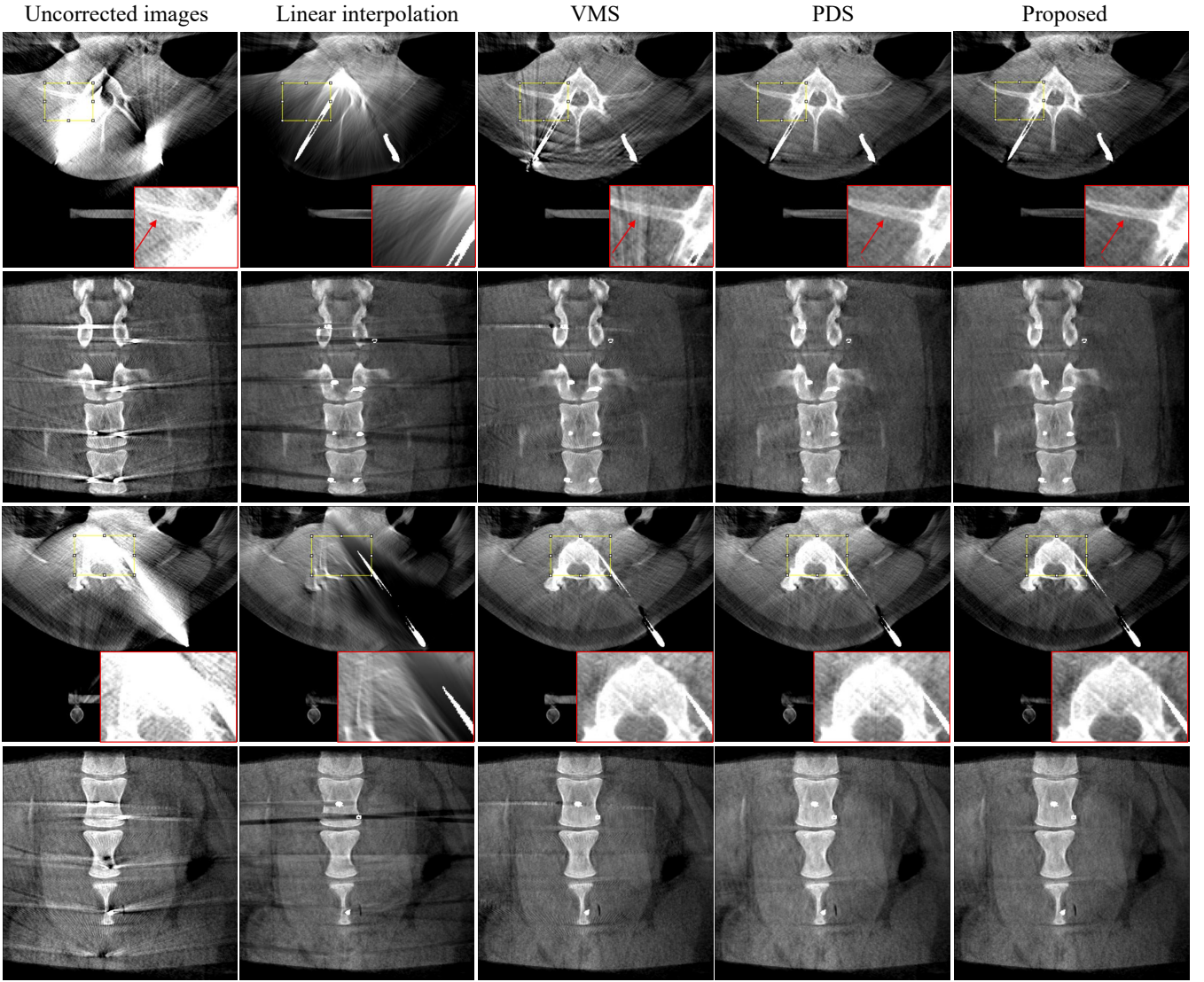


Fig. 11. MAR results in tomographic and sagittal views for spinal nailing in comparison experiments on real datasets. Rows 1 and 2 show the MAR results for Slice 1, and rows 3 and 4 show the MAR results for Slice 2. The display window is [250, 1200] HU.

method achieved the most effective suppression of metal artifacts among the evaluated techniques. It also demonstrated superior preservation of tissue details in regions surrounding the metal implants. The results in Slice 1 highlight the ability of the proposed method to maintain ROI integrity, particularly around the bone structures. Similarly, Slice 2 results confirm its capacity to address the bright-spot issues in the vertebral region caused by residual artifacts. Overall, the proposed method achieved the best balance between metal artifact suppression and preservation of anatomical structures.

Fig. 12 presented a comparative analysis of different MAR results applied to a CT slice of a spinal vertebra model. The uncorrected image displayed significant metal artifacts that severely obstructed the visualization of surrounding bony structures. These artifacts, characterized by pronounced streak patterns, created distinct disruptions in the anatomical details of the vertebra. When linear interpolation techniques were employed, artifact correction achieved only partial success, leaving considerable residual streaks around the metallic regions. This method also introduced secondary artifacts, causing substantial loss of soft tissue details near the metallic implants. Such limitations underscored the inadequacy of linear interpolation for clinical applications requiring high anatomical fidelity. In comparison, the VMS method demonstrated a certain level of improvement, as it resulted in a noticeable reduction in artifact intensity while preserving more surrounding tissue information. Nonetheless, residual artifacts remained visible, particularly in regions of high attenuation gradients, as indicated by the arrow in Fig. 12. The VMS method exhibited a modest enhancement in visual quality, aligning with the performance reported in similar studies. However, the processed image still revealed an evident loss of critical details, particularly in fine anatomical structures, which restricted its clinical utility. The PDS achieved further improvements, effectively reducing the residual streak artifacts. As

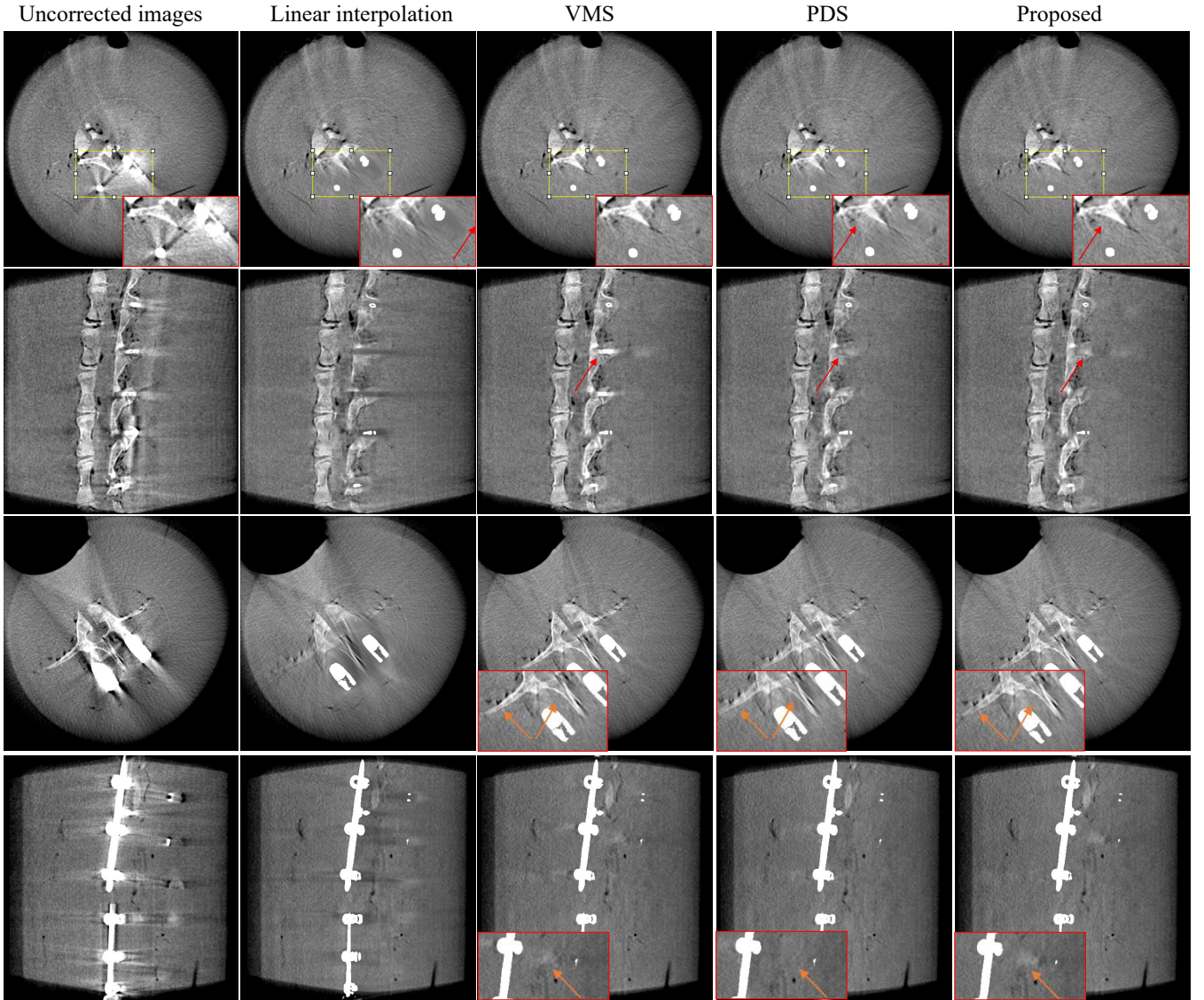


Fig. 12. MAR results in tomographic and sagittal views for vertebral arch model in comparison experiments on real datasets. Rows 1 and 2 show the MAR results for Slice 1, and rows 3 and 4 show the MAR results for Slice 2. The display window is [60, 750] HU.

265 shown in Fig.12, the PDS approach preserved a greater amount of anatomical detail compared to VMS, especially in the  
 266 regions highlighted by the arrow, where residual artifacts were less prominent. The superior performance of PDS in artifact  
 267 suppression and tissue preservation highlighted its potential as an effective MAS technique. Despite these advancements, subtle  
 268 inaccuracies persisted in low-contrast regions, indicating the presence of challenges in handling complex attenuation variations.  
 269 In contrast to above methods, the proposed method, as applied to the simulated dataset, demonstrated superior performance  
 270 in both artifact suppression and preservation of critical anatomical details. The method achieved nearly complete removal of  
 271 metal artifacts, as evidenced by the absence of visible streaks around metallic implants and the preservation of fine details in  
 272 the surrounding tissue.

273 In summary, the conclusions from the real and simulated datasets indicated a significant improvement over other techniques,  
 274 underscoring the robustness and effectiveness of the proposed approach. The findings emphasized the potential of this method  
 275 to address the longstanding challenges in MAR, making it a promising candidate for integration into clinical workflows aimed  
 276 at improving diagnostic accuracy in the presence of metallic implants.

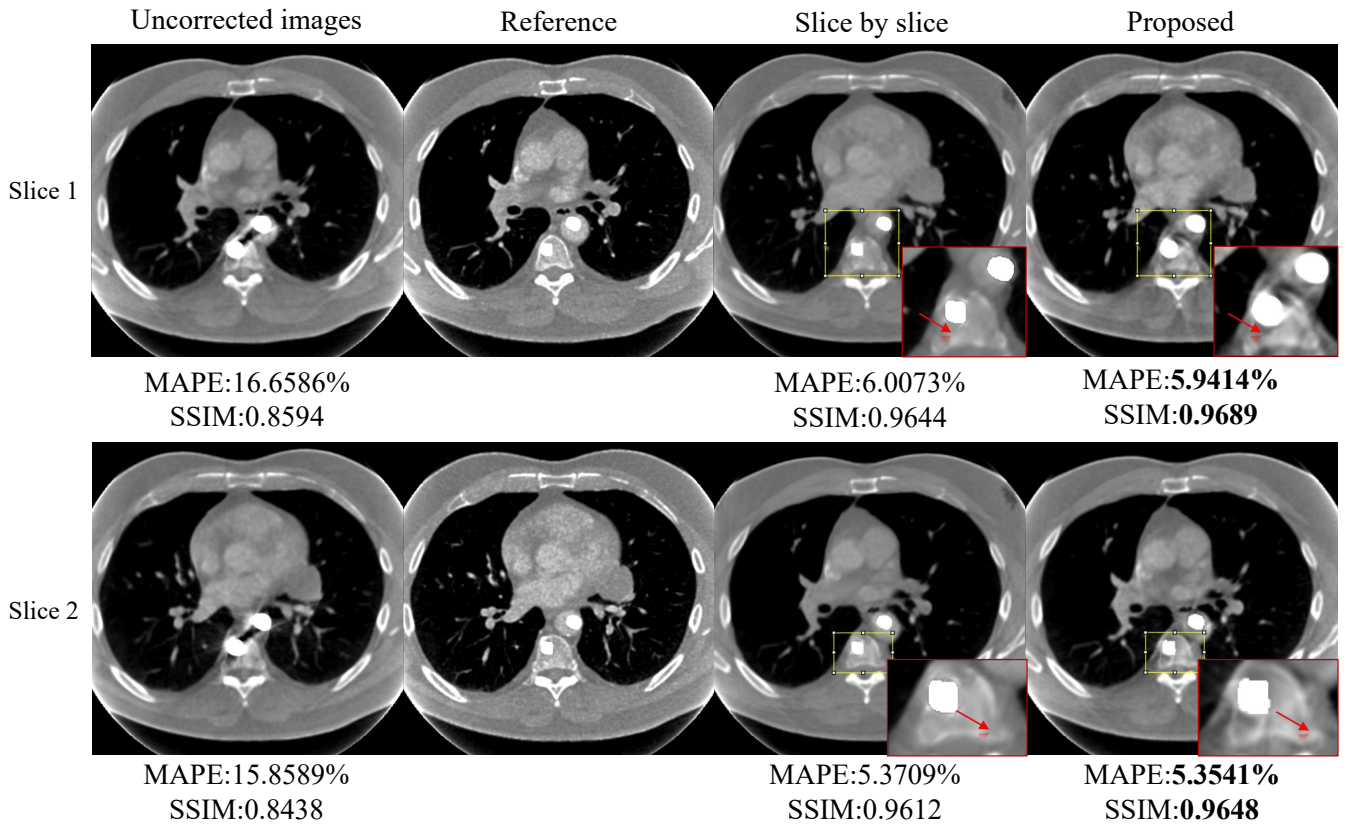


Fig. 13. MAR results for the slice-by-slice approach and the proposed method for vertebral arch model. Starting from the reference image, uncorrected image, and MAR-processed results. The display window is [80, 100] HU.

277

## 2. Comparison with the MAR method of slice-by-slice processing

278 The proposed method directly suppressed metal artifacts in the three-dimensional projection domain. To evaluate its performance, a comparative analysis was conducted against the image-domain MAR method based on slice-by-slice processing. 279 Fig.13 illustrates the results obtained from the simulated dataset using both the proposed approach and the image-domain MAR 280 method on two CBCT reconstructed slices of the same volume. It was evident that severe beam-hardening streak artifacts 281 persisted between the two metal implants in the uncorrected image, leading to a significant loss of structural information around 282 the spinal region. The image-domain MAR method partially mitigated these artifacts, but its ability to recover fine anatomical 283 details was notably insufficient in certain regions, such as the area around the vertebral edges in slice 1. Quantitative evaluation 284 further highlighted the superiority of the proposed method in terms of structural similarity and absolute percentage error, as 285 evidenced by the metrics achieving lower error indices than the slice-by-slice MAR method. 286

287 Fig.14 presented the experimental results obtained from clinical data by comparing the proposed method and the slice-by- 288 slice MAR method on two reconstructed slices from the same CBCT volume. Due to the lack of a ground-truth reference for 289 clinical datasets, the evaluation relied on visual assessments and indirect comparisons to the baseline images. Severe metal 290 artifacts in the uncorrected images significantly disrupted the visualization of fine anatomical details, particularly in the region 291 indicated by the arrow in slice2. The slice-by-slice MAR method suppressed the artifacts to a certain extent but introduced 292 simulated structural deformations, such as loss of spinal detail in the same region. In contrast, the proposed method achieved 293 effective artifact suppression while preserving anatomical structures and soft tissue details, as demonstrated in the corrected 294 images.

295 In summary, the proposed method consistently outperformed the image-domain MAR method in both simulated and clinical 296 datasets. It exhibited robust capabilities in achieving superior artifact suppression, maintaining structural integrity, and mini- 297 mizing quantitative evaluation errors. These findings demonstrated the potential of the proposed approach to achieve reliable 298 and accurate diagnostic analysis while addressing the challenges of metal artifact suppression in clinical CBCT imaging.

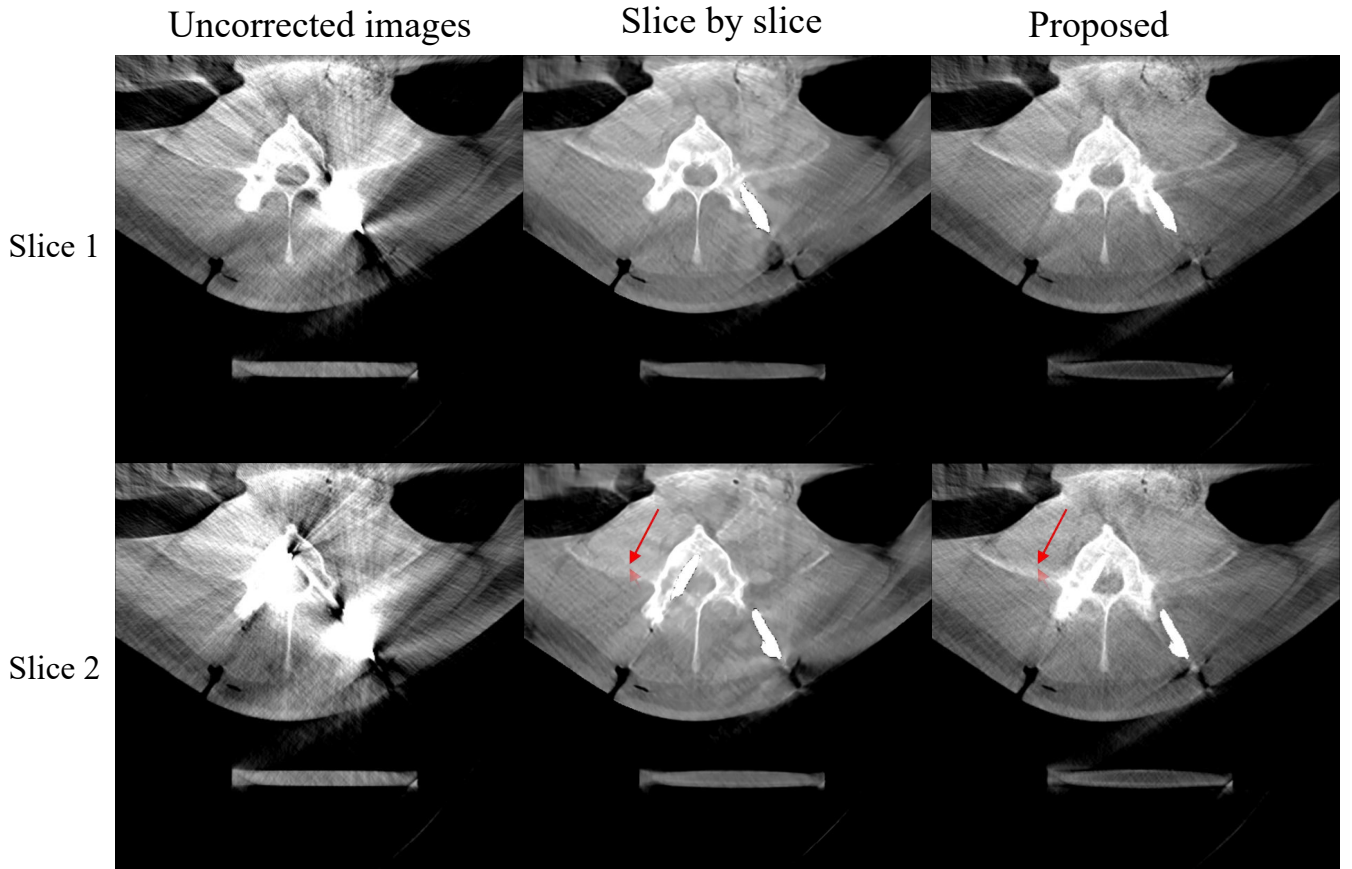


Fig. 14. MAR results for the layer-by-layer approach and the proposed method for spinal nails. Starting from the reference image, uncorrected image, and MAR-processed results. The display window is [80, 100] HU.

299

#### D. Results and analysis of ablation experiments

300

##### 1. Contribution of morphological refinement post-processing to metal artifact suppression after metal projection segmentation

301 The contribution of the segmentation-based post-processing refinement in suppressing metal artifacts in projection data was  
 302 highlighted in this study. Fig.15 demonstrated a comparative analysis involving three sets of images derived from clinical  
 303 datasets. It was evident from Fig.15 that the uncorrected images in the first column had exhibited severe metal artifacts that  
 304 obscured the surrounding anatomical structures, particularly around metallic implants. Such artifacts had severely compro-  
 305 mised clinical diagnostics by making it challenging to evaluate the condition of adjacent tissues. The images in the second  
 306 column, which had relied solely on interpolation-based correction informed by segmentation outcomes without further refine-  
 307 ment, revealed a partial reduction in artifact intensity. Although the metal artifacts had been mitigated to some extent, residual  
 308 distortions and inaccuracies had persisted, especially in critical regions such as the edges of vertebrae. These residual arti-  
 309 facts had continued to impede accurate tissue characterization and diagnostic reliability. The third column demonstrated the  
 310 results obtained by incorporating the proposed segmentation-based post-processing refinement. This approach had effectively  
 311 addressed the limitations of prior methods by leveraging refined segmentation to guide projection-domain corrections, result-  
 312 ing in a substantial suppression of metal artifacts. Compared to interpolation-based correction, the refinement process had  
 313 significantly reduced residual streaks and distortions, as illustrated in the visually improved anatomical structures and more  
 314 distinguishable soft tissue regions. Quantitative assessments had further reinforced these observations, showcasing superior  
 315 performance metrics for the proposed method in comparison to its predecessors. The results clearly underlined the critical role  
 316 of segmentation-based refinement in suppressing projection-domain metal artifacts.

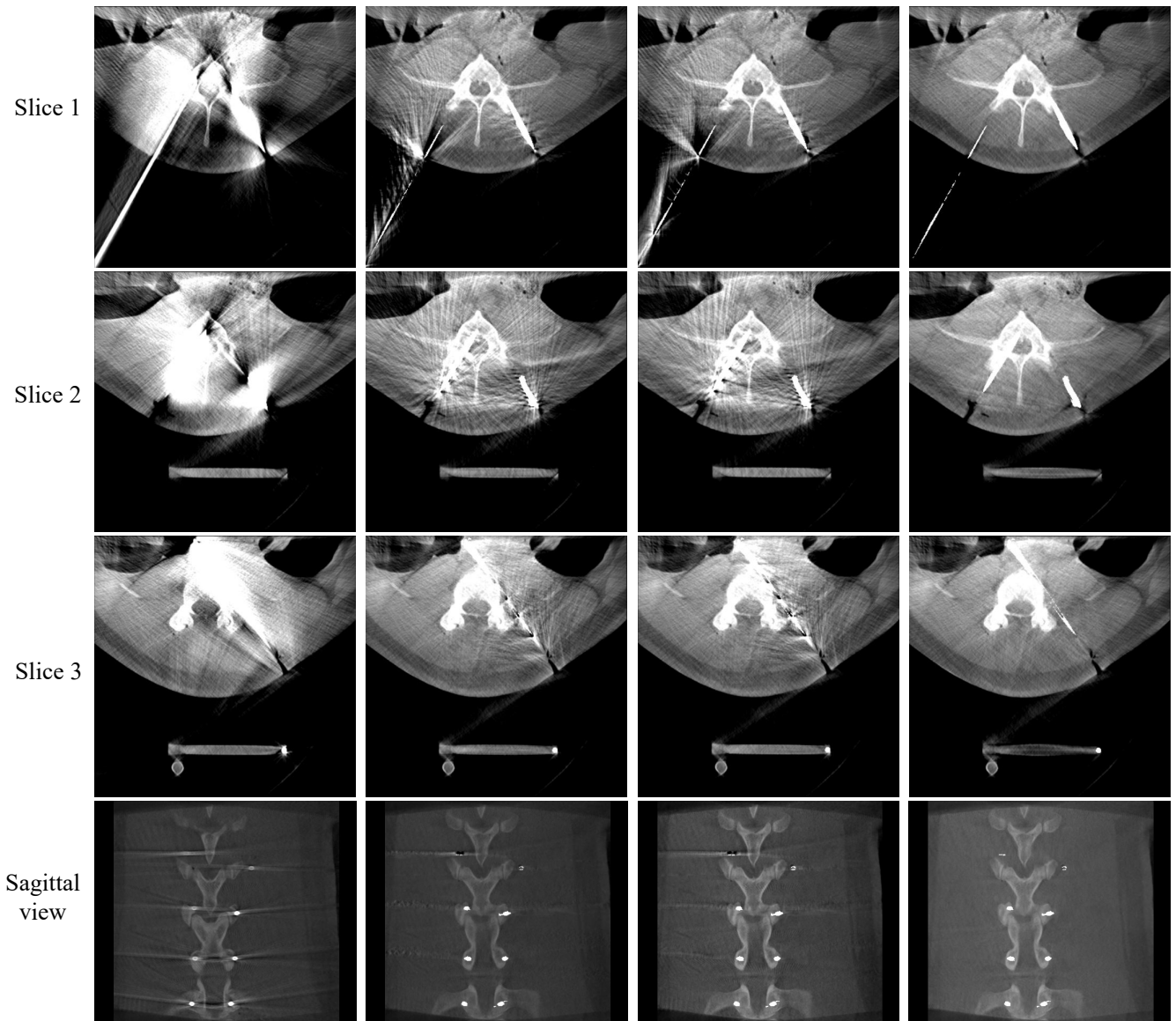


Fig. 15. Contribution of morphological refinement post-processing to metal artifact suppression after metal projection segmentation. The first column represents uncorrected images, the second column includes images corrected using interpolation based on segmentation results, and the third column depicts images processed through the proposed segmentation-refinement method. Rows 1–3 correspond to axial slices extracted from three different reconstructed volumes. The display window is [70, 1000] HU.

317

## 2. Contribution of two-dimensional Delaunay triangulation interpolation to metal artifact suppression

318 A comparison of MAR methods based on different interpolation techniques was performed using a clinical dataset of two  
 319 cases. For each case, two processing methods and one cross-sectional image at a defect site were selected for analysis. Fig.16  
 320 illustrated the results obtained from the application of various interpolation-based approaches on clinical datasets. It had been  
 321 observed that the NMAR method failed to adequately suppress metal artifacts in these cases. The residual streak artifacts  
 322 surrounding metallic implants had introduced significant errors during the diagnostic process, as the projection data contained  
 323 residual streaking and secondary artifacts. As shown in the axial slice in Fig.16, NMAR processing had introduced additional  
 324 secondary streaks, leading to degraded image quality that was only marginally improved compared to uncorrected images. This  
 325 could be attributed to the limitations of NMAR in accounting for spatial continuity in three-dimensional volumetric imaging.  
 326 As a result, the NMAR algorithm had exhibited suboptimal artifact suppression, failing to preserve detailed structural infor-  
 327 mation around metallic objects and leaving residual streaks visible in critical anatomical regions. In contrast, the proposed  
 328 interpolation-based approach demonstrated superior performance in suppressing metal artifacts. The proposed method not only

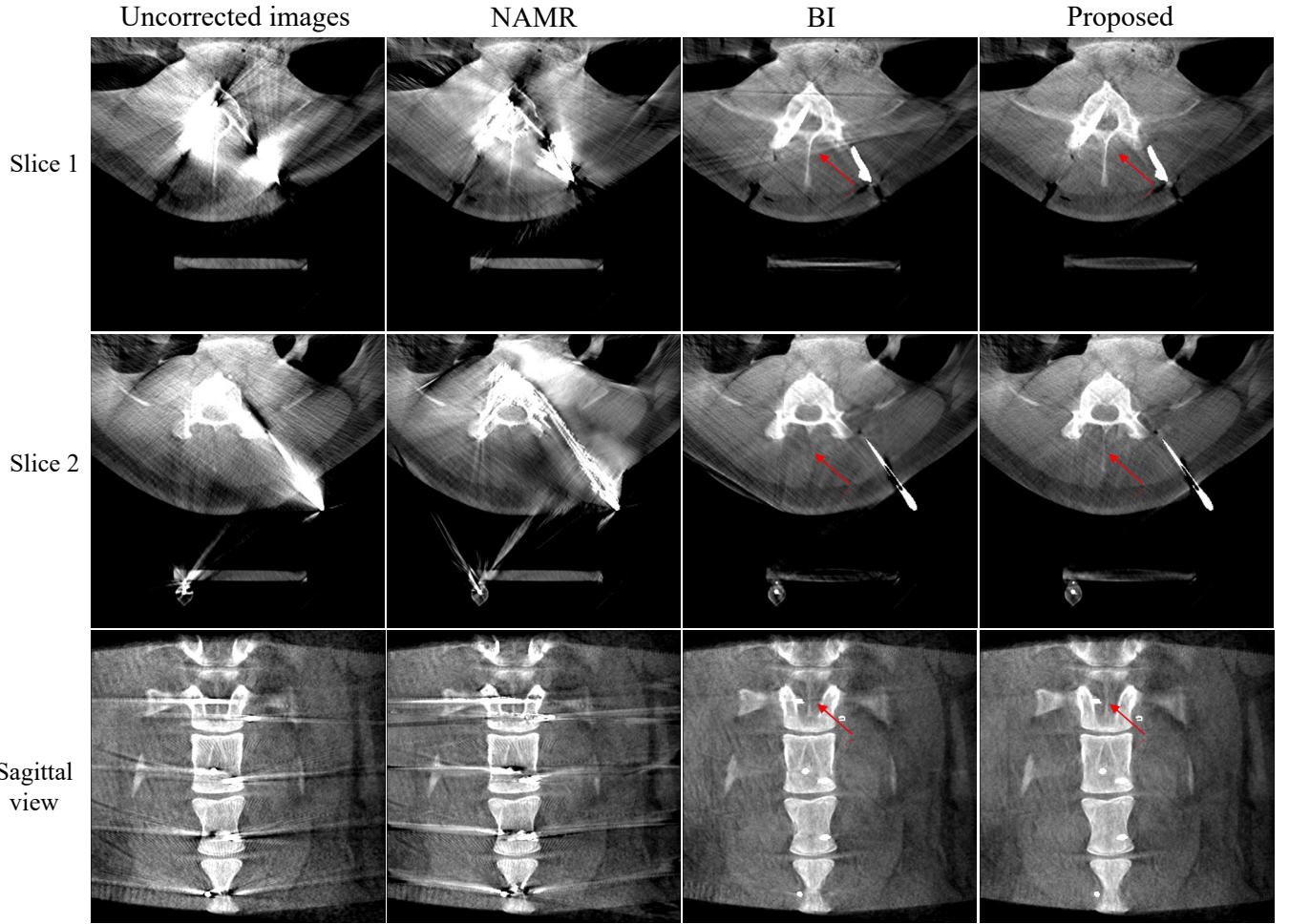


Fig. 16. Results of MAR performed on spinal nails using normalized interpolation correction, Boreman interpolation (BI) and wo-dimensional Delaunay triangulation interpolation. The display window is [80, 800] HU.

329 conserved the rich details around the metal after processing the metal artifacts, but also left few residual artifacts when viewed  
 330 from the sagittal view. Fig.17 presented the results of the MAR processing from two simulated datasets. The reconstructed  
 332 images in the NMAR-processed slices retained prominent streak artifacts, as seen in Fig.17. The NMAR algorithm had failed  
 333 to recover essential structural details within high-density regions, primarily due to the absence of iterative corrections for spatial  
 334 inconsistencies in the projection data. Consequently, this method introduced significant visual distortions in the reconstructed  
 335 images, making it unsuitable for accurate diagnostic interpretation.

336 In contrast, the proposed method achieved a more comprehensive suppression of metal artifacts in the simulated datasets. As  
 337 evident in Fig.17, streak artifacts were almost entirely eliminated, with clearer visualization of the bony structures and soft tis-  
 338 sues surrounding the metallic implants. The interpolation refinement had contributed to superior anatomical fidelity, effectively  
 339 resolving residual streaks that were otherwise prominent in the NMAR-processed images. The cross-sectional analysis further  
 340 corroborated these findings, with negligible residual artifacts observed at defect sites. This demonstrated the robustness and  
 341 generalizability of the proposed method in addressing projection-domain inconsistencies while preserving structural integrity.  
 342 In summary, the proposed MAR method exhibited significant advantages over NMAR by achieving enhanced suppression of  
 343 metal artifacts and preserving essential structural information, making it well-suited for clinical and simulated datasets. The  
 344 experimental results highlighted its potential to provide artifact-free imaging for accurate diagnostic purposes.

345

#### E. Time cost analysis

346 The computational performance of the proposed method was evaluated and compared with independent scattering correc-  
 347 tion and metallic segmentation networks, as shown in Tab.3. The evaluation metrics included computational time, parameter

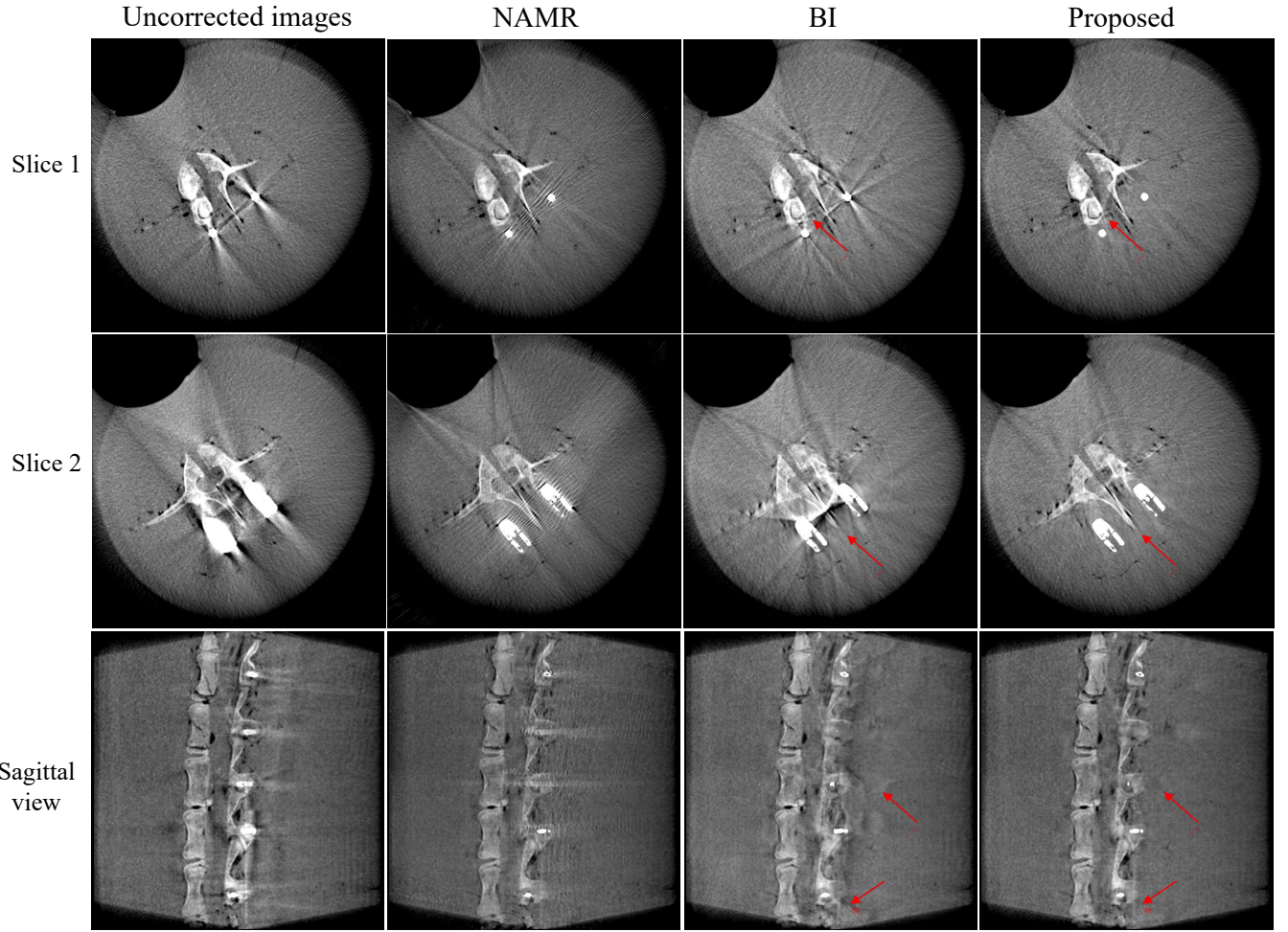


Fig. 17. Results of MAR performed on vertebral arch model using normalized interpolation correction, Boreman interpolation (BI) and two-dimensional Delaunay triangulation interpolation. The display window is [60, 750] HU.

348 count, and floating-point operations (FLOPs). For the scattering correction network, the computation time required per pro-  
 349 jection image was 0.0486 s, with a parameter count of 8.751 M and 26.421 G FLOPs. The metallic segmentation network  
 350 demonstrated significantly faster computation at 0.0051 s per projection, with 0.863 M parameters and 30.413 G FLOPs. For  
 351 the hybrid method that integrates scattering correction and metallic segmentation, the combined network achieved an inference  
 352 time of 0.0492 s, parameter count of 9.513 M, and required 23.371 G FLOPs. These results demonstrated a notable trade-off  
 353 between computational cost and efficiency in the hybrid approach. When comparing the computational performance of the

TABLE 3. Performance Evaluation of Scattering and Segmentation Combined Processing.

Method	Computation Time (s)	Parameters (M)	FLOPs (G)
Scattering Estimation Network	0.0486	8.751	26.421
Metallic Segmentation Network	0.0051	0.863	30.413
Step-by-Step	0.0537	9.614	-
The proposed	0.0492	9.513	23.371

354 individual networks with the hybrid approach, several advantages of the hybrid model were observed. Although the scattering  
 355 correction network and metallic segmentation network independently demonstrated fast computation and low parameter counts,  
 356 the integration of these functionalities in the hybrid model reduced redundant computations, achieving greater efficiency. The  
 357 slight increase in parameter count from 8.751 M (scattering correction) to 9.513 M (hybrid model) was justified by the re-  
 358 duced FLOPs and enhanced integration capabilities. The hybrid model also demonstrated a notable reduction in computational  
 359 overhead. While the independent networks required 0.0537 s in combined processing time per projection image, the hybrid  
 360 approach completed the task in 0.0492 s, representing a significant performance improvement. This efficiency gain was at-

363 tributed to the unified architecture, which minimized data transfer and eliminated redundant computations between the two  
 364 separate tasks. Furthermore, the reduction in FLOPs from 30.413 G (metallic segmentation network) and 26.421 G (scattering  
 365 correction network) to 23.371 G in the hybrid model highlighted its computational advantage. By merging the two networks,  
 366 the hybrid approach reduced the need for excessive memory and computational resources while maintaining high accuracy  
 367 in processing. These results underscored the hybrid model's suitability for clinical applications requiring real-time metal  
 368 artifact reduction in CT imaging. The hybrid design effectively preserved the scattering correction and metallic segmentation  
 369 functionalities, enabling improved artifact suppression with reduced computational burden. Its optimized parameter count and  
 370 computation time positioned it as a reliable solution for large-scale data processing and real-time imaging workflows. In sum-  
 371 mary, the hybrid network architecture provided a computationally efficient and accurate approach for metal artifact reduction.  
 372 Its ability to integrate scattering correction and segmentation tasks while minimizing computational costs and processing time  
 373 represented a significant advancement in the field.

374

#### IV. DISCUSSION AND CONCLUSION

375 In this article, we developed an end-to-end MAR method that incorporates both scattering correction and metal segmentation  
 376 in the projection domain in the same network. After obtaining the metal projection segmentation results are then refined to  
 377 deal with the accurate and continuous metal masks that are incorrectly labeled as metal projections for subsequent interpolation  
 378 algorithms, and finally the reconstructed metal artifacts are eliminated using Delaunay triangular interpolation. In this paper,  
 379 actual scanned pedicle nail models and clinical spinal nail data from Jiangsu First Image's equipment were used. Compared  
 380 to the method of removing metal artifacts by performing slice-by-slice metal artifact removal from CBCT data, the method  
 381 proposed in this paper takes into account the correlation between each slice and is able to maximize the elimination of metal  
 382 artifacts observed from coronal and sagittal views. The results of the ablation experiments demonstrated that increasing the  
 383 accuracy of the scattering correction promoted the metal artifact suppression effect, while improving the fidelity of some details  
 384 of the tissue and the contrast of the overall image, and that the Delaunay triangular interpolation metal artifact suppression  
 385 method after the introduction of the metal projection segmentation also improved the metal artifact suppression effect both  
 386 qualitatively and quantitatively. Although the APP-Net demonstrates encouraging improvement for MAR, some issues remain  
 387 to be noticed. **Limitation:** (1)The scatter correction network is not computationally efficient enough because the network uses  
 388 Pytorch's own Fourier package for the computation of the Fourier transform, which may reduce the computational efficiency.  
 389 (2)The diversity of the data in the dataset is not rich enough. Due to the complexity of the real imaging system and the  
 390 variety of metal shapes, there is a lack of a rich collection of metal CBCT projections (diversity of metal sizes, materials,  
 391 etc.) to further optimize the network to meet the needs of different scenarios. **Future research:** (1)Multi-modal Imaging  
 392 Integration: Combining CBCT data with other imaging modalities, such as MRI or PET, to further improve metal artifact  
 393 suppression and diagnostic accuracy. (2)Real-Time Processing: Optimizing the framework for real-time applications through  
 394 model compression and hardware acceleration. (3)Generalizability: Expanding the dataset to include diverse clinical scenarios,  
 395 enabling robust performance across various implant types and anatomical regions. (4)Patient-Specific Models: Developing  
 396 adaptive models that account for individual patient anatomy and implant characteristics, enhancing clinical applicability.

397

#### V. REFERENCES

- 
- 398 [1] Jia Hao, Li Zhang, Liang Li, Zhiqiang Chen, and Kejun Kang. A practical image reconstruction and processing method for symmetrically  
 399 off-center detector cbct system. *Nuclear Science and Techniques*, 24(4), 2013.
- 400 [2] Kai Chen, Li-Bo Zhang, Jia-Shun Liu, Yuan Gao, Zhan Wu, Hai-Chen Zhu, Chang-Ping Du, Xiao-Li Mai, Chun-Feng Yang, and Yang  
 401 Chen. Robust restoration of low-dose cerebral perfusion ct images using ncs-unet. *Nuclear Science and Techniques*, 33(3):30, 2022.
- 402 [3] Cui Zhang, Xiao Dong Pan, and Gong Ping Shang. Improvements to conventional x-ray tube-based cone-beam computed tomography  
 403 system. *nuclear science and techniques*, 29(3), 2018.
- 404 [4] Hong Kai Yang, Kai Chao Liang, Ke Jun Kang, and Yu Xiang Xing. Slice-wise reconstruction for low-dose cone-beam ct using a deep  
 405 residual convolutional neural network. *Nuclear Science and Techniques*, 30(04):28–36, 2019.
- 406 [5] Xing Yue Ruan, Xiu Fang Li, Meng Ya Guo, Mei Chen, Ming Lv, Rui Li, and Zhi Ling Chen. Cone-beam computed tomography  
 407 noise reduction method based on u-net with convolutional block attention module in proton therapy. *Nuclear Science and Techniques*,  
 408 35(7):89–100, 2024.
- 409 [6] Wenjun Zhang, Haining Ding, Hongchun Xu, MingMing Jin, and Gang Huang. An unsupervised deep learning network model for  
 410 artifact correction of cone-beam computed tomography images. *Biomedical Signal Processing and Control*, 95:106362, 2024.

- 411 [7] Chen Wang, Jingyu Yang, Baoyu Wu, Ruijun Liu, and Peng Yu. Trans-vnet: Transformer-based tooth semantic segmentation in cbct  
 412 images. *Biomedical Signal Processing and Control*, 97:106666, 2024.
- 413 [8] Min Yuan, Yufei Xie, Rongchang Zhao, Ningning Lv, Zijian Zhang, Liye Zhu, and Xiaolin Wu. Generating synthesized computed  
 414 tomography from cbct/lct using a novel generative-transformer adversarial-cnn. *Biomedical Signal Processing and Control*, 96:106660,  
 415 2024.
- 416 [9] Fuqiang Yang, Dinghua Zhang, Hua Zhang, and Kuidong Huang. Cupping artifacts correction for polychromatic x-ray cone-beam com-  
 417 puted tomography based on projection compensation and hardening behavior. *Biomedical Signal Processing and Control*, 57:101823,  
 418 2020.
- 419 [10] Andre Mouton, Najla Megherbi, Katrien Van Slambrouck, Johan Nuysts, and Toby P Breckon. An experimental survey of metal artefact  
 420 reduction in computed tomography. *Journal of X-ray Science and Technology*, 21(2):193–226, 2013.
- 421 [11] Willi A Kalender, Robert Hebel, and Johannes Ebersberger. Reduction of ct artifacts caused by metallic implants. *Radiology*,  
 422 164(2):576–577, 1987.
- 423 [12] Jikun Wei, Laigao Chen, George A Sandison, Yun Liang, and Lisa X Xu. X-ray ct high-density artefact suppression in the presence of  
 424 bones. *Physics in Medicine & Biology*, 49(24):5407, 2004.
- 425 [13] Esther Meyer, Rainer Raupach, Michael Lell, Bernhard Schmidt, and Marc Kachelrieß. Normalized metal artifact reduction (nmr) in  
 426 computed tomography. *Medical physics*, 37(10):5482–5493, 2010.
- 427 [14] Esther Meyer, Rainer Raupach, Bernhard Schmidt, Andreas H Mahnken, and Marc Kachelrieß. Adaptive normalized metal artifact  
 428 reduction (anmr) in computed tomography. In *2011 IEEE Nuclear Science Symposium Conference Record*, pages 2560–2565. IEEE,  
 429 2011.
- 430 [15] Peter Bannas, Yinseng Li, Utaroh Motosugi, Ke Li, Meghan Lubner, Guang-Hong Chen, and Perry J Pickhardt. Prior image constrained  
 431 compressed sensing metal artifact reduction (piccs-mar): 2d and 3d image quality improvement with hip prostheses at ct colonography.  
 432 *European radiology*, 26:2039–2046, 2016.
- 433 [16] Ge Wang, Donald L Snyder, Joseph A O’Sullivan, and Michael W Vannier. Iterative deblurring for ct metal artifact reduction. *IEEE  
 434 transactions on medical imaging*, 15(5):657–664, 1996.
- 435 [17] Pieter EB Vaissier, Marlies C Goorden, Aaron B Taylor, and Freek J Beekman. Fast count-regulated osem reconstruction with adaptive  
 436 resolution recovery. *IEEE transactions on medical imaging*, 32(12):2250–2261, 2013.
- 437 [18] Zhiqian Chang, Dong Hye Ye, Somesh Srivastava, Jean-Baptiste Thibault, Ken Sauer, and Charles Bouman. Prior-guided metal artifact  
 438 reduction for iterative x-ray computed tomography. *IEEE transactions on medical imaging*, 38(6):1532–1542, 2018.
- 439 [19] Gengsheng L Zeng. A projection-domain iterative algorithm for metal artifact reduction by minimizing the total-variation norm and the  
 440 negative-pixel energy. *Visual Computing for Industry, Biomedicine, and Art*, 5(1):1, 2022.
- 441 [20] Kai Chen, Zhengyuan Zhou, Yuchen Li, Xu Ji, Jiasong Wu, Jean-Louis Coatrieux, Yang Chen, and Gouenou Coatrieux. Red-net:  
 442 Residual and enhanced discriminative network for image steganalysis in the internet of medical things and telemedicine. *IEEE Journal  
 443 of Biomedical and Health Informatics*, 28(3):1611–1622, 2023.
- 444 [21] Kai Chen, Yang Chen, Gouenou Coatrieux, Jiasong Wu, and Jean Louis Coatrieux. Restoration-enhanced reversible information  
 445 steganography network for ct images in the internet of medical things. *IEEE Transactions on Instrumentation and Measurement*,  
 446 PP.
- 447 [22] Kai Chen, Guohui Ji, Chenrui Wang, Zhiguang Peng, Xu Ji, Hui Tang, Chunfeng Yang, and Yang Chen. Ct-net: Cascaded t-shape  
 448 network using spectral redundancy for dual-energy ct limited-angle reconstruction. *Biomedical signal processing and control*, 2023.
- 449 [23] Kai Chen, Tianling Lyu, Jean Louis Coatrieux, and Yang Chen. Dual-energy ct metal artifact reduction by combined material decom-  
 450 position and projection domain threshold segmentation. In *ICASSP 2025 - 2025 IEEE International Conference on Acoustics, Speech and  
 451 Signal Processing (ICASSP)*.
- 452 [24] Muhammad Usman Ghani and W Clem Karl. Fast enhanced ct metal artifact reduction using data domain deep learning. *IEEE  
 453 Transactions on Computational Imaging*, 6:181–193, 2019.
- 454 [25] Haofu Liao, Wei-An Lin, Zhimin Huo, Levon Vogelsang, William J Sehnert, S Kevin Zhou, and Jiebo Luo. Generative mask pyramid  
 455 network for ct/cbct metal artifact reduction with joint projection-sinogram correction. In *Medical Image Computing and Computer  
 456 Assisted Intervention–MICCAI 2019: 22nd International Conference, Shenzhen, China, October 13–17, 2019, Proceedings, Part VI* 22,  
 457 pages 77–85. Springer, 2019.
- 458 [26] Yulin Zhu, Hanqing Zhao, Tangsheng Wang, Lei Deng, Yupeng Yang, Yuming Jiang, Na Li, Yinping Chan, Jingjing Dai, Chulong  
 459 Zhang, et al. Sinogram domain metal artifact correction of ct via deep learning. *Computers in Biology and Medicine*, 155:106710, 2023.
- 460 [27] Haofu Liao, Wei-An Lin, S Kevin Zhou, and Jiebo Luo. Adn: artifact disentanglement network for unsupervised metal artifact reduction.  
 461 *IEEE Transactions on Medical Imaging*, 39(3):634–643, 2019.
- 462 [28] Ge Wang, Jong Chu Ye, Klaus Mueller, and Jeffrey A Fessler. Image reconstruction is a new frontier of machine learning. *IEEE  
 463 transactions on medical imaging*, 37(6):1289–1296, 2018.
- 464 [29] Xia Huang, Jian Wang, Fan Tang, Tao Zhong, and Yu Zhang. Metal artifact reduction on cervical ct images by deep residual learning.  
 465 *Biomedical engineering online*, 17:1–15, 2018.
- 466 [30] Yanbo Zhang and Hengyong Yu. Convolutional neural network based metal artifact reduction in x-ray computed tomography. *IEEE  
 467 transactions on medical imaging*, 37(6):1370–1381, 2018.
- 468 [31] Hong Wang, Yuexiang Li, Haimiao Zhang, Deyu Meng, and Yefeng Zheng. Indudonet+: A deep unfolding dual domain network for  
 469 metal artifact reduction in ct images. *Medical Image Analysis*, 85:102729, 2023.
- 470 [32] Bo Zhou, Xiongchao Chen, S Kevin Zhou, James S Duncan, and Chi Liu. Dudodr-net: Dual-domain data consistent recurrent network  
 471 for simultaneous sparse view and metal artifact reduction in computed tomography. *Medical Image Analysis*, 75:102289, 2022.
- 472 [33] Yuanyuan Lyu, Wei-An Lin, Haofu Liao, Jingjing Lu, and S Kevin Zhou. Encoding metal mask projection for metal artifact reduc-  
 473 tion in computed tomography. In *Medical Image Computing and Computer Assisted Intervention–MICCAI 2020: 23rd International*

- 474 *Conference, Lima, Peru, October 4–8, 2020, Proceedings, Part II 23*, pages 147–157. Springer, 2020.
- 475 [34] Lequan Yu, Zhicheng Zhang, Xiaomeng Li, and Lei Xing. Deep sinogram completion with image prior for metal artifact reduction in ct  
476 images. *IEEE transactions on medical imaging*, 40(1):228–238, 2020.
- 477 [35] Wei-An Lin, Haofu Liao, Cheng Peng, Xiaohang Sun, Jingdan Zhang, Jiebo Luo, Rama Chellappa, and Shaohua Kevin Zhou. Dudonet:  
478 Dual domain network for ct metal artifact reduction. In *Proceedings of the IEEE/CVF Conference on Computer Vision and Pattern  
479 Recognition*, pages 10512–10521, 2019.
- 480 [36] Yiannis Kyriakou, Esther Meyer, Daniel Prell, and Marc Kachelrieß. Empirical beam hardening correction (ebhc) for ct. *Medical  
481 physics*, 37(10):5179–5187, 2010.
- 482 [37] Tristan M Gottschalk, Andreas Maier, Florian Kordon, and Björn W Kreher. View-consistent metal segmentation in the projection  
483 domain for metal artifact reduction in cbct—an investigation of potential improvement. *arXiv preprint arXiv:2112.02101*, 2021.